Azimuthal anisotropy in Cu+Au collisions at $\sqrt{s_{NN}} = 200$ GeV

L. Adamczyk,[1] J. R. Adams,[29] J. K. Adkins,[19] G. Agakishiev,[17] M. M. Aggarwal,[31] Z. Ahammed,[54] N. N. Ajitanand,[42] I. Alekseev,[15,26] D. M. Anderson,[44] R. Aoyama,[48] A. Aparin,[17] D. Arkhipkin,[3] E. C. Aschenauer,[3] M. U. Ashraf,[47] A. Attri,[31] G. S. Averichev,[17] X. Bai,[7] V. Bairathi,[27] K. Barish,[50] A. Behera,[42] R. Bellwied,[46] A. Bhasin,[16] A. K. Bhati,[31] P. Bhattarai,[45] J. Bielcik,[10] J. Bielcikova,[11] L. C. Bland,[3] I. G. Bordyuzhin,[15] J. Bouchet,[18] J. D. Brandenburg,[36] A. V. Brandin,[26] D. Brown,[23] J. Bryslawskyj,[50] I. Bunzarov,[17] J. Butterworth,[36] H. Caines,[58] M. Calderón de la Barca Sánchez,[5] J. M. Campbell,[29] D. Cebra,[5] I. Chakaberia,[3,18,40] P. Chaloupka,[10] Z. Chang,[44] N. Chankova-Bunzarova,[17] A. Chatterjee,[54] S. Chattopadhyay,[54] X. Chen,[21] J. H. Chen,[41] X. Chen,[39] J. Cheng,[47] M. Cherney,[9] W. Christie,[3] G. Contin,[22] H. J. Crawford,[4] S. Das,[7] T. G. Dedovich,[17] J. Deng,[40] I. M. Deppner,[51] A. A. Derevschikov,[33] L. Didenko,[3] C. Dilks,[32] X. Dong,[22] J. L. Drachenberg,[20] J. E. Draper,[5] J. C. Dunlop,[3] L. G. Efimov,[17] N. Elsey,[56] J. Engelage,[4] G. Eppley,[36] R. Esha,[6] S. Esumi,[48] O. Evdokimov,[8] J. Ewigleben,[23] O. Eyser,[3] R. Fatemi,[19] S. Fazio,[3] P. Federic,[11] P. Federicova,[10] J. Fedorisin,[17] Z. Feng,[7] P. Filip,[17] E. Finch,[49] Y. Fisyak,[3] C. E. Flores,[5] J. Fujita,[9] L. Fulek,[1] C. A. Gagliardi,[44] F. Geurts,[36] A. Gibson,[53] M. Girard,[55] D. Grosnick,[53] D. S. Gunarathne,[43] Y. Guo,[18] A. Gupta,[16] W. Guryn,[3] A. I. Hamad,[18] A. Hamed,[44] A. Harlenderova,[10] J. W. Harris,[58] L. He,[34] S. Heppelmann,[5] S. Heppelmann,[32] N. Herrmann,[51] A. Hirsch,[34] S. Horvat,[58] X. Huang,[47] H. Z. Huang,[6] T. Huang,[28] B. Huang,[8] T. J. Humanic,[29] P. Huo,[42] G. Igo,[6] W. W. Jacobs,[14] A. Jentsch,[45] J. Jia,[3,42] K. Jiang,[39] S. Jowzaee,[56] E. G. Judd,[4] S. Kabana,[18] D. Kalinkin,[14] K. Kang,[47] D. Kapukchyan,[50] K. Kauder,[56] H. W. Ke,[3] D. Keane,[18] A. Kechechyan,[17] Z. Khan,[8] D. P. Kikoła,[55] C. Kim,[50] I. Kisel,[12] A. Kisiel,[55] L. Kochenda,[26] M. Kocmanek,[11] T. Kollegger,[12] L. K. Kosarzewski,[55] A. F. Kraishan,[43] L. Krauth,[50] P. Kravtsov,[26] K. Krueger,[2] N. Kulathunga,[46] L. Kumar,[31] J. Kvapil,[10] J. H. Kwasizur,[14] R. Lacey,[42] J. M. Landgraf,[3] K. D. Landry,[6] J. Lauret,[3] A. Lebedev,[3] R. Lednicky,[17] J. H. Lee,[3] W. Li,[41] C. Li,[39] X. Li,[39] Y. Li,[47] J. Lidrych,[10] T. Lin,[14] M. A. Lisa,[29] F. Liu,[7] P. Liu,[42] Y. Liu,[44] H. Liu,[14] T. Ljubicic,[3] W. J. Llope,[56] M. Lomnitz,[22] R. S. Longacre,[3] S. Luo,[8] X. Luo,[7] G. L. Ma,[41] R. Ma,[3] Y. G. Ma,[41] L. Ma,[41] N. Magdy,[42] R. Majka,[58] D. Mallick,[27] S. Margetis,[18] C. Markert,[45] H. S. Matis,[22] D. Mayes,[50] K. Meehan,[5] J. C. Mei,[40] Z. W. Miller,[8] N. G. Minaev,[33] S. Mioduszewski,[44] D. Mishra,[27] S. Mizuno,[22] B. Mohanty,[27] M. M. Mondal,[13] D. A. Morozov,[33] M. K. Mustafa,[22] Md. Nasim,[6] T. K. Nayak,[54] J. M. Nelson,[4] D. B. Nemes,[58] M. Nie,[41] G. Nigmatkulov,[26] T. Niida,[56] L. V. Nogach,[33] T. Nonaka,[48] S. B. Nurushev,[33] G. Odyniec,[22] A. Ogawa,[3] K. Oh,[35] V. A. Okorokov,[26] D. Olvitt Jr.,[43] B. S. Page,[3] R. Pak,[3] Y. Pandit,[8] Y. Panebratsev,[17] B. Pawlik,[30] H. Pei,[7] C. Perkins,[4] J. Pluta,[55] K. Poniatowska,[55] J. Porter,[22] M. Posik,[43] A. M. Poskanzer,[22] N. K. Pruthi,[31] M. Przybycien,[1] J. Putschke,[56] A. Quintero,[43] S. Ramachandran,[19] R. L. Ray,[45] R. Reed,[23] M. J. Rehbein,[9] H. G. Ritter,[22] J. B. Roberts,[36] O. V. Rogachevskiy,[17] J. L. Romero,[5] J. D. Roth,[9] L. Ruan,[3] J. Rusnak,[11] O. Rusnakova,[10] N. R. Sahoo,[44] P. K. Sahu,[13] S. Salur,[37] J. Sandweiss,[58] M. Saur,[11] J. Schambach,[45] A. M. Schmah,[22] W. B. Schmidke,[3] N. Schmitz,[24] B. R. Schweid,[42] J. Seger,[9] M. Sergeeva,[6] R. Seto,[50] P. Seyboth,[24] N. Shah,[41] E. Shahaliev,[17] P. V. Shanmuganathan,[23] M. Shao,[39] W. Q. Shen,[41] S. S. Shi,[7] Z. Shi,[22] Q. Y. Shou,[41] E. P. Sichtermann,[22] R. Sikora,[1] M. Simko,[11] S. Singha,[18] M. J. Skoby,[14] N. Smirnov,[58] D. Smirnov,[3] W. Solyst,[14] P. Sorensen,[3] H. M. Spinka,[2] B. Srivastava,[34] T. D. S. Stanislaus,[53] D. J. Stewart,[58] M. Strikhanov,[26] B. Stringfellow,[34] A. A. P. Suaide,[38] T. Sugiura,[48] M. Sumbera,[11] B. Summa,[32] X. Sun,[7] Y. Sun,[39] X. M. Sun,[7] B. Surrow,[43] D. N. Svirida,[15] Z. Tang,[39] A. H. Tang,[3] A. Taranenko,[26] T. Tarnowsky,[25] A. Tawfik,[57] J. Thäder,[22] J. H. Thomas,[22] A. R. Timmins,[46] D. Tlusty,[36] T. Todoroki,[3] M. Tokarev,[17] S. Trentalange,[6] R. E. Tribble,[44] P. Tribedy,[3] S. K. Tripathy,[13] B. A. Trzeciak,[10] O. D. Tsai,[6] B. Tu,[7] T. Ullrich,[3] D. G. Underwood,[2] I. Upsal,[29] G. Van Buren,[3] G. van Nieuwenhuizen,[3] A. N. Vasiliev,[33] F. Videbæk,[3] S. Vokal,[17] S. A. Voloshin,[56] A. Vossen,[14] G. Wang,[6] F. Wang,[34] Y. Wang,[7] Y. Wang,[47] G. Webb,[3] J. C. Webb,[3] L. Wen,[6] G. D. Westfall,[25] H. Wieman,[22] S. W. Wissink,[14] R. Witt,[52] Y. Wu,[18] Z. G. Xiao,[47] G. Xie,[39] W. Xie,[34] Q. H. Xu,[40] Y. F. Xu,[41] J. Xu,[7] N. Xu,[22] Z. Xu,[3] C. Yang,[40] S. Yang,[3] Q. Yang,[40] Y. Yang,[28] Z. Ye,[8] Z. Ye,[8] L. Yi,[58] K. Yip,[3] I.-K. Yoo,[35] N. Yu,[7] H. Zbroszczyk,[55] W. Zha,[39] J. B. Zhang,[7] J. Zhang,[22] S. Zhang,[39] L. Zhang,[7] J. Zhang,[21] X. P. Zhang,[47] Z. Zhang,[41] S. Zhang,[41] Y. Zhang,[39] J. Zhao,[34] C. Zhong,[41] C. Zhou,[41] L. Zhou,[39] X. Zhu,[47] Z. Zhu,[40] and M. Zyzak[12]

(STAR Collaboration)

[1]*AGH University of Science and Technology, FPACS, Cracow 30-059, Poland*

[2]*Argonne National Laboratory, Argonne, Illinois 60439*

[3]*Brookhaven National Laboratory, Upton, New York 11973*

[4]*University of California, Berkeley, California 94720*

[5]*University of California, Davis, California 95616*

[6]*University of California, Los Angeles, California 90095*

[7]*Central China Normal University, Wuhan, Hubei 430079*

[8]*University of Illinois at Chicago, Chicago, Illinois 60607*

[9]*Creighton University, Omaha, Nebraska 68178*

[10]*Czech Technical University in Prague, FNSPE, Prague 115 19, Czech Republic*

[11]*Nuclear Physics Institute ASCR, Prague 250 68, Czech Republic*

[12]*Frankfurt Institute for Advanced Studies FIAS, Frankfurt 60438, Germany*

[13]*Institute of Physics, Bhubaneswar 751005, India*

[14]*Indiana University, Bloomington, Indiana 47408*
[15]*Alikhanov Institute for Theoretical and Experimental Physics, Moscow 117218, Russia*
[16]*University of Jammu, Jammu 180001, India*
[17]*Joint Institute for Nuclear Research, Dubna 141 980, Russia*
[18]*Kent State University, Kent, Ohio 44242*
[19]*University of Kentucky, Lexington, Kentucky 40506-0055*
[20]*Lamar University, Physics Department, Beaumont, Texas 77710*
[21]*Institute of Modern Physics, Chinese Academy of Sciences, Lanzhou, Gansu 730000*
[22]*Lawrence Berkeley National Laboratory, Berkeley, California 94720*
[23]*Lehigh University, Bethlehem, Pennsylvania 18015*
[24]*Max-Planck-Institut fur Physik, Munich 80805, Germany*
[25]*Michigan State University, East Lansing, Michigan 48824*
[26]*National Research Nuclear University MEPhI, Moscow 115409, Russia*
[27]*National Institute of Science Education and Research, HBNI, Jatni 752050, India*
[28]*National Cheng Kung University, Tainan 70101*
[29]*Ohio State University, Columbus, Ohio 43210*
[30]*Institute of Nuclear Physics PAN, Cracow 31-342, Poland*
[31]*Panjab University, Chandigarh 160014, India*
[32]*Pennsylvania State University, University Park, Pennsylvania 16802*
[33]*Institute of High Energy Physics, Protvino 142281, Russia*
[34]*Purdue University, West Lafayette, Indiana 47907*
[35]*Pusan National University, Pusan 46241, Korea*
[36]*Rice University, Houston, Texas 77251*
[37]*Rutgers University, Piscataway, New Jersey 08854*
[38]*Universidade de Sao Paulo, Sao Paulo, 05314-970, Brazil*
[39]*University of Science and Technology of China, Hefei, Anhui 230026*
[40]*Shandong University, Jinan, Shandong 250100*
[41]*Shanghai Institute of Applied Physics, Chinese Academy of Sciences, Shanghai 201800*
[42]*State University of New York, Stony Brook, New York 11794*
[43]*Temple University, Philadelphia, Pennsylvania 19122*
[44]*Texas A&M University, College Station, Texas 77843*
[45]*University of Texas, Austin, Texas 78712*
[46]*University of Houston, Houston, Texas 77204*
[47]*Tsinghua University, Beijing 100084*
[48]*University of Tsukuba, Tsukuba, Ibaraki 305-8571, Japan*
[49]*Southern Connecticut State University, New Haven, Connecticut 06515*
[50]*University of California, Riverside, California 92521*
[51]*University of Heidelberg, Heidelberg 69120, Germany*
[52]*United States Naval Academy, Annapolis, Maryland 21402*
[53]*Valparaiso University, Valparaiso, Indiana 46383*
[54]*Variable Energy Cyclotron Centre, Kolkata 700064, India*
[55]*Warsaw University of Technology, Warsaw 00-661, Poland*
[56]*Wayne State University, Detroit, Michigan 48201*
[57]*World Laboratory for Cosmology and Particle Physics (WLCAPP), Cairo 11571, Egypt*
[58]*Yale University, New Haven, Connecticut 06520*

(Received 5 December 2017; published 31 July 2018)

The azimuthal anisotropic flow of identified and unidentified charged particles has been systematically studied in Cu+Au collisions at $\sqrt{s_{NN}} = 200$ GeV for harmonics $n = 1$–4 in the pseudorapidity range $|\eta| < 1$. The directed flow in Cu+Au collisions is compared with the rapidity-odd and, for the first time, the rapidity-even components of charged particle directed flow in Au+Au collisions at $\sqrt{s_{NN}} = 200$ GeV. The slope of the directed flow pseudorapidity dependence in Cu+Au collisions is found to be similar to that in Au+Au collisions, with the intercept shifted toward positive pseudorapidity values, i.e., the Cu-going direction. The mean transverse momentum projected onto the spectator plane $\langle p_x \rangle$ in Cu+Au collision also exhibits approximately linear dependence on pseudorapidity with the intercept at about $\eta \approx -0.4$ (shifted from zero in the Au-going direction), closer to the rapidity of the Cu+Au system center of mass. The observed dependencies find a natural explanation in a picture of the directed flow originating partly due the "tilted source" and partly due to the asymmetry in

the initial density distribution. A charge dependence of $\langle p_x \rangle$ was also observed in Cu+Au collisions, consistent with an effect of the initial electric field created by charge difference of the spectator protons in two colliding nuclei. The rapidity-even component of directed flow in Au+Au collisions is close to that in Pb+Pb collisions at $\sqrt{s_{NN}} = 2.76$ TeV, indicating a similar magnitude of dipolelike fluctuations in the initial-state density distribution. Higher harmonic flow in Cu+Au collisions exhibits similar trends to those observed in Au+Au and Pb+Pb collisions and is qualitatively reproduced by a viscous hydrodynamic model and a multiphase transport model. For all harmonics with $n \geqslant 2$ we observe an approximate scaling of v_n with the number of constituent quarks; this scaling works as well in Cu+Au collisions as it does in Au+Au collisions.

DOI: 10.1103/PhysRevC.98.014915

I. INTRODUCTION

The study of the azimuthal anisotropic flow in relativistic heavy-ion collisions has been making valuable contributions to the exploration of the properties of the hot and dense matter—quark-gluon plasma (QGP)—created in such collisions. Anisotropic flow is usually characterized by the coefficients v_n in the Fourier expansion of the particle azimuthal distribution measured relative to the so-called flow symmetry planes: $dN/d\phi \propto 1 + 2\sum_n v_n \cos[n(\phi - \Psi_n)]$, where ϕ is the azimuthal angle of a produced particle, and Ψ_n is the azimuthal angle of the nth-harmonic flow plane. The first harmonic (directed flow) and second harmonic (elliptic flow) coefficients have been measured most often and compared to the theoretical models [1–3]. According to recent theoretical calculations, the higher harmonic flow coefficients appear to provide additional and sometimes even stronger constraints on the QGP models and on the initial conditions in heavy-ion collisions [4,5].

Elliptic flow v_2 has been extensively studied both at the Relativistic Heavy Ion Collider (RHIC) and the Large Hadron Collider (LHC) energies. For low transverse momentum ($p_T < 2$ GeV/c), $v_2(p_T)$ is well described by the viscous hydrodynamic models. A comparison of the elliptic flow measurement to hydrodynamic model calculations led to the finding that the QGP created in nuclear collisions at RHIC and LHC energies has an extremely small ratio of shear viscosity to entropy density, η/s, and behaves as an almost ideal liquid [2–4]. The centrality dependence of elliptic flow, and in particular flow fluctuations, provided detailed information on the initial conditions and their fluctuations.

While the experimental results on the elliptic flow are mostly understood, there exists no single model that satisfactorily explains the directed flow dependencies on centrality, collision energy, system size, rapidity, transverse momentum, and even more, on the particle type [1]. This clearly indicates that an important piece in our picture of ultrarelativistic collisions is still missing. This could affect many conclusions made solely on the elliptic flow measurements, as the initial conditions that would be required for a satisfactory description of the directed flow could lead to stronger (or weaker) elliptic flow. Possible effects of that have been mostly ignored so far in part due to complication of 3+1 hydrodynamical calculations compared to 2+1 calculations assuming Bjorken scaling. The directed flow originates in the initial-state spatial and momentum (initial collective velocity fields) asymmetries in the transverse plane. The directed flow might be intimately related to the vorticity in the system, and via that to the global polarization of the system and to chirality flow—two of the most intriguing directions in current heavy ion research [6,7].

The RHIC has been very successful in providing data on symmetric collisions of approximately spherical nuclei such as Cu+Cu and Au+Au, and nonspherical nuclei such as U+U, as well as asymmetric Cu+Au collisions. Since the anisotropic flow originates from the anisotropy of the initial density distribution in the overlap region of the colliding nuclei, these collisions provide important complementary information on both the geometry and fluctuations in the initial density distributions. In particular, Cu+Au collisions are characterized by a large asymmetry in the average initial density distribution in the transverse plane, leading to significant v_1 and v_3 flow coefficients even at midrapidity. Measurements of v_1 and v_3 in Cu+Au collisions can be compared to the corresponding measurements in symmetric collisions, where they can originate only in density fluctuations, thus providing additional information on the role of the initial density gradients. Asymmetric collisions, with their strong electric fields in the initial stages due to the charge difference of spectator protons in the colliding nuclei, offer a unique opportunity to study the electric conductivity of the created matter and provide access to the time development of quark and antiquark production [8–11].

In symmetric collisions, such as Au+Au, the directed flow measured relative to the reaction plane (a plane defined by the impact parameter vector and the beam direction) is an odd function of (pseudo)rapidity. Note that while in symmetric collisions there exist an ambiguity/freedom in which of the nuclei is called a projectile and which is a target, there is not any ambiguity in the results. The impact parameter is always defined as a vector in the transverse plane from the center of the target nucleus to the center of the projectile nucleus. The projectile velocity defines the positive z direction, and, correspondingly, positive (pseudo)rapidity. The directed flow measured relative to the reaction plane has a characteristic "$\sim$" shape, crossing zero three times, with negative slope at midrapidity (for a review, see [1]), where the sign of the directed flow is conventionally defined to be positive for projectile spectators at forward rapidity. The origin of such a dependence is not totally clear. In hydrodynamic models, it is often produced through "tilted" source initial conditions [12–14], as shown in Fig. 1(a), with parameters of the tilt obtained from a fit to the data [14,15]. In a pure "tilted source" scenario [12,13], $v_1(p_T)$ is a monotonic function of p_T and the pseudorapidity dependence of $\langle p_x \rangle(\eta) \equiv \langle p_T \cos(\phi - \Psi_1) \rangle$, where $\langle\rangle$ means an average over particles in an event and then an average over all events, can be directly related to that of $v_1(\eta)$

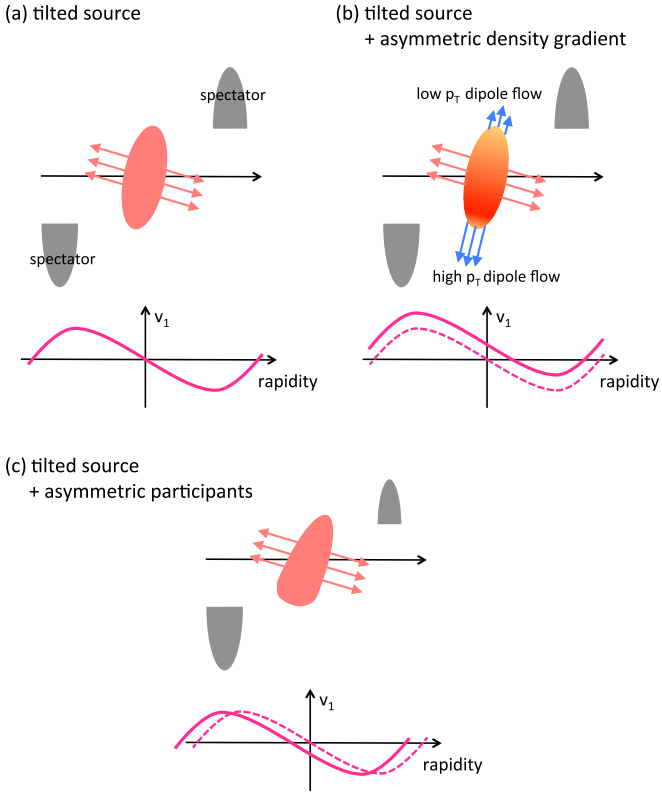

FIG. 1. Cartoon illustrating different contributions to the directed flow and their effect on the (pseudo)rapidity dependence of mean v_1. Panel (a) shows the effect of the "tilted source," while panels (b) and (c) include additional effects of asymmetric density distribution and asymmetry in number of participating nucleons. In panels (b) and (c), the dashed lines represent the effect of the "tilted source" only and the solid lines represent the two effects combined.

(see the Appendix). In asymmetric collisions, as well as in symmetric collisions away from midrapidity, the initial transverse density distribution has dipolelike asymmetry. This leads to an additional contribution to anisotropic flow, interpreted either as shadowing [16], or due to the difference in pressure gradients in different directions within the transverse plane [17]. The first harmonic term, often called dipole flow after a dipolelike density asymmetry, contributes to directed flow. The sign of the dipole flow contribution appears to be similar to that of "tilted source." However there exists a significant difference between the two contributions—the contribution to $\langle p_x \rangle$ from dipole flow is zero [18]. This fact can be used to disentangle the relative contributions to directed flow from the "tilted source" and initial density asymmetries. The condition $\langle p_x \rangle^{\rm dipole} = 0$ also leads to a characteristic $v_1^{\rm dipole}(p_T)$ shape which crosses zero at $p_T \sim \langle p_T \rangle$ [18]. Higher p_T particles tend to be emitted in this direction, while lower p_T particles are emitted in the opposite direction to balance the momentum in the system. The sign of the average contribution to v_1 is determined by the low p_T particles.

The fluctuations in the initial density distribution, in particular those leading to a dipole asymmetry in the transverse plane, lead to nonzero directed flow, i.e., dipole flow, even at midrapidity [18]. The direction (azimuthal angle) of the initial dipole asymmetry $\Psi_1^{\rm dipole}$ determines the direction of flow. The dipole flow angle $\Psi_1^{\rm dipole}$ can be approximated by $\Psi_{1,3} = \arctan(\langle r^3 \sin\phi \rangle / \langle r^3 \cos\phi \rangle) + \pi$ [18] where r and ϕ are the polar coordinates of participants and a weighted average is taken over the overlap region of two nuclei, with the weight being the energy or entropy density. The angle $\Psi_{1,3}$ points in the direction of the largest density gradient. Very schematically, the modification to $v_1(\eta)$ for a particular fluctuation leading to positive dipole flow is shown in Fig. 1(b).

The difference in the number of participating nucleons (quarks) in the projectile and target nuclei also leads to the change in rapidity of the "fireball" center of mass relative to that of nucleon-nucleon system. In symmetric collisions such a difference would be a consequence of fluctuations in the number of participating nucleons event by event [19], while in asymmetric collisions the position of the center of mass of participating nucleons will be shifted on average, depending on centrality. In this case, one would expect the overall shape of $v_1(\eta)$ to be mostly unchanged, but the entire $v_1(\eta)$ curve to be shifted in the direction of rapidity where more participants move, as schematically indicated in Fig. 1(c).

Finally, we note that the dipole flow is found to be less sensitive to the shear viscosity over entropy η/s [20] than v_2 and v_3, therefore it provides a better constraint on the geometry and fluctuations of the system in the initial state.

In Pb+Pb and Au+Au collisions the initial dipolelike asymmetry in the density distribution at midrapidity is caused purely by the fluctuations, while Cu+Au collisions have an intrinsic density asymmetry due to the asymmetric size of colliding nuclei. In addition to the directed flow of the "tilted source" [Fig. 1(a)], one might expect the dipole flow to be produced by the asymmetric density gradient [Fig. 1(b)] and the center-of-mass shift in asymmetric collisions [Fig. 1(c)]. Therefore it is of great interest to study the different components of directed flow in Cu+Au collisions to improve our understanding of the role of gradients in the initial density distributions and the hydrodynamic response to such an initial state.

Experimentally, the directed flow is often studied with the first harmonic event plane determined by the spectator neutrons [21–23]. Recent study [10] shows that in ultrarelativistic nuclear collisions the spectators on average deflect outward from the center of the collision, e.g., projectile spectators deflect in the direction of the impact parameter vector. By combining the measurements relative to the projectile $\Psi_{\rm SP}^p$ and target $\Psi_{\rm SP}^t$ spectator planes, the ALICE Collaboration reported the rapidity-odd and even components of directed flow in Pb+Pb collisions at $\sqrt{s_{NN}} = 2.76$ TeV [24]:

$$v_1 = v_1^{\rm odd} + v_1^{\rm even}, \tag{1}$$

$$v_1^{\rm odd} = \left(v_1\{\Psi_{\rm SP}^p\} - v_1\{\Psi_{\rm SP}^t\}\right)/2, \tag{2}$$

$$v_1^{\rm even} = \left(v_1\{\Psi_{\rm SP}^p\} + v_1\{\Psi_{\rm SP}^t\}\right)/2, \tag{3}$$

where the "even" component might originate in the fluctuation of the initial density. Note that the "projectile" nucleus defines the forward direction and $\langle \cos(\Psi_{\rm SP}^p - \Psi_{\rm SP}^t) \rangle < 0$. Since the target spectator plane $\Psi_{\rm SP}^t$ points in the opposite direction to $\Psi_{\rm SP}^p$, in the ALICE paper [24], directed flow relative to the target spectator plane was defined as $v_1\{\Psi_{\rm SP}^t\} = -\langle \cos(\phi - \Psi_{\rm SP}^t) \rangle$,

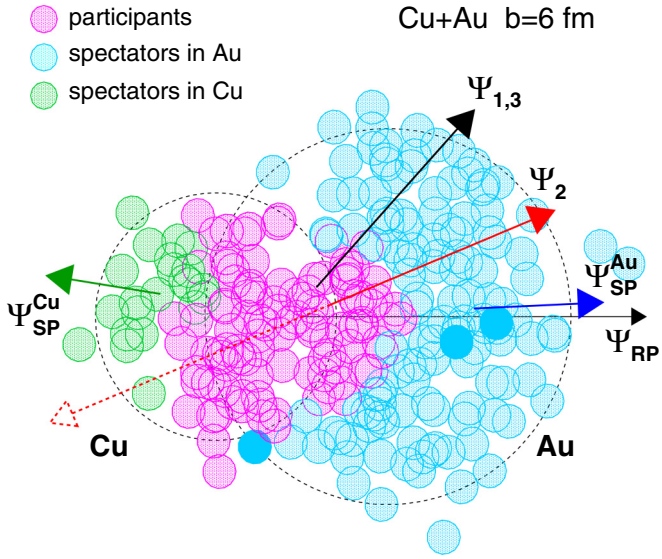

FIG. 2. Cartoon of Cu+Au collision indicating different event planes used in the analysis. Note that Ψ_2 and $\Psi_2 + \pi$ define the same plane.

resulting in Eqs. (2) and (3) having the opposite sign convention from Ref. [24].

A finite v_1^{even} was observed in Pb+Pb collisions with little if any rapidity dependence [24]. It is believed that the origin of this component is in finite correlations between the direction of spectator plane and the direction of the initial dipole asymmetry at midrapidity. Such a correlation is expected to be weak, $\langle\cos(\Psi_{\text{SP}}^{p} - \Psi_{1,3})\rangle \ll 1$, which would explain the small magnitude of v_1^{even} of the order of a few per mil. The v_1^{dipole} can be measured via two-particle correlation (v_1^{dipole} relative to participant plane) [25,26] taking into account the momentum conservation effect which requires model-dependent treatment. The v_1^{dipole} measured using two-particle correlation [25] shows ~40 times larger magnitude than v_1^{even} measured with spectator planes. This difference can be explained by the weak correlation of $\langle\cos(\Psi_{\text{SP}}^{p} - \Psi_{1,3})\rangle$ as discussed in Ref. [24].

Following a similar approach to that of ALICE Collaboration, we study directed flow in midrapidity region relative to the target (Au) and projectile (Cu) spectator planes (see Fig. 2). We identify two components of the directed flow: the one determined by the directed flow relative to the (true) reaction plane Ψ_{RP}, and the component due to the initial density fluctuations. The first component is similar to the "odd" component in symmetric collisions, but in Cu+Au collisions it also includes a contribution due to nonzero average dipolelike asymmetry in the initial density distribution. The second component, due to the initial density fluctuations, is similar to the "even" component in the ALICE analysis. In addition to the results obtained from correlations to the spectator planes, we also present the results from three-particle correlations [3,21,27], $v_1\{3\}$, which are interpreted as a projection of the directed flow onto the second harmonic event plane Ψ_2 that is defined by participants. See the schematic view of a collision with different event planes identified in Fig. 2. Model calculations [18] suggest that the dipole flow might be correlated more strongly with Ψ_2 (second harmonic participant event plane) than with the spectator plane (which is very close to the reaction plane), and thus one can expect that the dipole flow contribution to $v_1\{3\}$ might be slightly larger than that with the spectator plane.

Elliptic and higher harmonic flow measurements in asymmetric collisions are also extremely interesting. While in symmetric collisions, the odd harmonics originate from the initial density fluctuations [28], in asymmetric collisions the intrinsic geometrical asymmetry in the initial state may lead to significant odd components of the flow. Thus the measurements of higher harmonic flow as well as the directed flow in Cu+Au collisions provide an opportunity to study the interplay of the two effects and provide additional constraints on hydrodynamic models.

A quark number scaling was observed for the elliptic flow [3,29,30], suggesting collective behavior at a partonic level. Recently PHENIX reported that the quark number scaling also works for higher harmonic flow in Au+Au collisions at $\sqrt{s_{NN}} =$ 200 GeV [31] by considering the order of the harmonics in the scaling rule, although the interpretation is still under discussion. It is very interesting to study if such a scaling is also held in asymmetric collisions having a potentially different origin for the odd component of the higher harmonic flow.

In this paper we present the measurements of the higher harmonic (up to $n = 4$) anisotropic flow of unidentified and identified charged particles in Cu+Au collisions. Results from Cu+Au collisions are compared with those from Au+Au collisions, as well as with hydrodynamic and transport models. We discuss the quark number scaling for v_2, v_3, and v_4 of charged pions, charged kaons, and (anti)protons. Compared to the previous measurements, a better accuracy of v_3 results and new data on v_4 provide a more detailed view on the scaling properties of anisotropic flow in asymmetric collisions and the physics behind it.

This paper is organized as follows: Section II provides a brief explanation of the experimental setup. The details of data reduction and analysis method are described in Sec. III. Results for the directed flow are presented in Sec. IV and results for higher harmonic flow are presented in Sec. V. For charged particles, we compare our results to theoretical models. For the higher harmonic flow of identified particles, we also discuss the number of constituent quark (NCQ) scaling. Section VI summarizes the results and findings.

II. EXPERIMENTAL SETUP

The STAR detector system is composed of central detectors performing tracking and particle identification, and trigger detectors located at the forward and backward directions. The zero degree calorimeters (ZDC) [32] and the vertex position detector (VPD) [33] are used to determine the minimum-bias trigger. The ZDCs are located at forward and backward angles of $|\eta| > 6.3$ and measure the energy deposit of spectator neutrons. The VPD consists of two identical detectors surrounding the beam pipe and covering the pseudorapidity range of $4.24 < |\eta| < 5.1$. The VPD provides the start time of the collision and the position of the collision vertex along the beam direction.

The time projection chamber (TPC) [34] is used for the tracking of charged particles. It covers the full azimuth and has an active pseudorapidity range of $|\eta| < 1$. The TPC is also used for particle identification via specific ionization energy loss, dE/dx. Particle identification also utilizes the time-of-flight detector (TOF) [35]. The TOF consists of multigap resistive plate chambers and covers the full azimuth and has a pseudorapidity range of $|\eta| < 0.9$. The timing resolution of the TOF system with the start time from the VPD is ∼100 ps.

III. DATA ANALYSIS

The analysis is based on the minimum-bias data for Cu+Au collisions at $\sqrt{s_{NN}} = 200$ GeV collected in 2012 and Au+Au collisions at $\sqrt{s_{NN}} = 200$ GeV collected in 2010. The collision vertex was required to be within ±30 cm from the center of the TPC in the beam direction. Additionally, the difference between the two z-vertex positions determined by TPC and VPD was required to be less than ±3 cm to reduce the beam-induced background (pileup). The vertex position in the transverse plane was required to be within 2 cm from the beam center. These criteria select 44 million minimum-bias triggered events for Cu+Au collisions and 95 million minimum-bias triggered events for Au+Au collisions. Centrality was defined based on the measured charged particle multiplicity within $|\eta| < 0.5$ and a Monte Carlo Glauber simulation in the same way as in previous studies [36]. The effect of the trigger efficiency was taken into account in the results by appropriate weights for both Cu+Au and Au+Au collisions.

In the following subsections, the details of analysis are described. Analysis procedures are basically the same as in previous STAR publications [27,37]. The only difference in the analysis between asymmetric and symmetric collisions is the way to evaluate the resolution of the event plane because one cannot assume equal subevents in forward and backward rapidities (two subevent method) in asymmetric collisions, as explained in Secs. III B and III C.

A. Track selection and particle identification

Good quality charged tracks were selected based on the TPC hit information as follows. The number of hit points used in track reconstruction was required to be greater than 14, with the maximum possible number of hit points of 45. The ratio of the number of hit points to the maximum possible for that track was required to be larger than 0.52. These requirements ensure better momentum resolution and allow us to avoid track splitting and merging effects. The track distance of closest approach to the primary vertex (DCA), was required to be less than 3 cm to reduce contributions from secondary decay particles. The tracks within $0.15 < p_T < 5$ GeV/c and $|\eta| < 1$ were analyzed in this study.

Particle identification was performed using the TPC and TOF information as mentioned above. For the TPC, the particles were identified based on the dE/dx distribution normalized by the expected energy loss given by the Bichsel function [38], expressed as $n\sigma^{\mathrm{TPC}} = \ln[(dE/dx)^{\mathrm{meas}}/(dE/dx)^{\mathrm{exp}}]/\delta_{dE/dx}$, where $\delta_{dE/dx}$ is the dE/dx resolution. The distribution of $n\sigma^{\mathrm{TPC}}$ is nearly Gaussian for a given momentum and is calibrated to be centered at zero with a width of unity for each particle species [39,40]. $\pi^+(\pi^-)$, $K^+(K^-)$, and $p(\bar{p})$ samples were obtained by requiring $|n\sigma^{\mathrm{TPC}}| < 2$ for particles of interest and $|n\sigma^{\mathrm{TPC}}| > 2$ for other particle species. To increase the purity of the kaon and proton samples, we applied the more stringent pion rejection requirement $|n\sigma^{\mathrm{TPC}}| > 3$. When the track has hit information from the TOF, the squared mass (m^2) can be calculated from the momentum, the time of flight, and the path length of the particle. The $\pi^+(\pi^-)$, $K^+(K^-)$, and $p(\bar{p})$ were selected from a 2σ window relative to their peaks in the m^2 distribution. Additionally the selected particles were required to be away from the m^2 peak for other particles. When the TOF information was used in the particle identification, the TPC selection criterion was relaxed to $|n\sigma^{\mathrm{TPC}}| < 3$ for the particle of interest. The purity of selected samples drops down to ∼90% at higher p_T. However we found that the variation of particle selection cuts does not affect the results beyond the uncertainties as described in Sec. III D.

B. Event plane determination

The event plane angles were reconstructed based on the following equations [3]:

$$n\Psi_n^{\mathrm{obs}} = \tan^{-1}\left(\frac{Q_{n,y}}{Q_{n,x}}\right), \tag{4}$$

$$Q_{n,x} = \sum_i w_i \cos(n\phi_i), \tag{5}$$

$$Q_{n,y} = \sum_i w_i \sin(n\phi_i), \tag{6}$$

where ϕ_i is the azimuthal angle of the charged track and w_i is the p_T weight (used only for the event plane determined in the TPC). The Ψ_n^{obs} is an estimated nth-order event plane and $Q_{n,x(y)}$ is referred to as the flow vector. Corrections for the detector acceptance were applied following Ref. [41]. The tracks measured in the TPC acceptance were divided into three subevents ($-1 < \eta < -0.4$, $|\eta| < 0.2$, and $0.4 < \eta < 1$). The track selection criteria mentioned above were applied but only tracks with $p_T < 2$ GeV/c were used for the event plane reconstruction.

The beam-beam counters (BBCs) [42] and the endcap-electromagnetic calorimeter (EEMC) [43] were also used for the event plane determination in addition to the TPC. The BBCs are located at forward and backward angles ($3.3 < |\eta| < 5$) and consist of scintillator tiles. When using the BBCs for the event plane determination, the azimuthal angle of the center of each tile was used for ϕ_i in Eqs. (7) and (8). and the ADC value in that tile was used as the weight w_i. The EEMC covers the pseudorapidity range of $1.086 < \eta < 2$ and consists of 720 towers (60×12 in the ϕ-η plane). When using the EEMC for the event plane determination, the azimuthal angle of each tower center was used as ϕ_i, and the transverse energy E_T was used as w_i. If E_T exceeded 2 GeV, a constant value of 2 was used as the weight.

For the first-order event plane, the ZDCs with shower maximum detectors (SMDs) [21] were used. Each SMD is composed of two planes with scintillator strips aligned with the

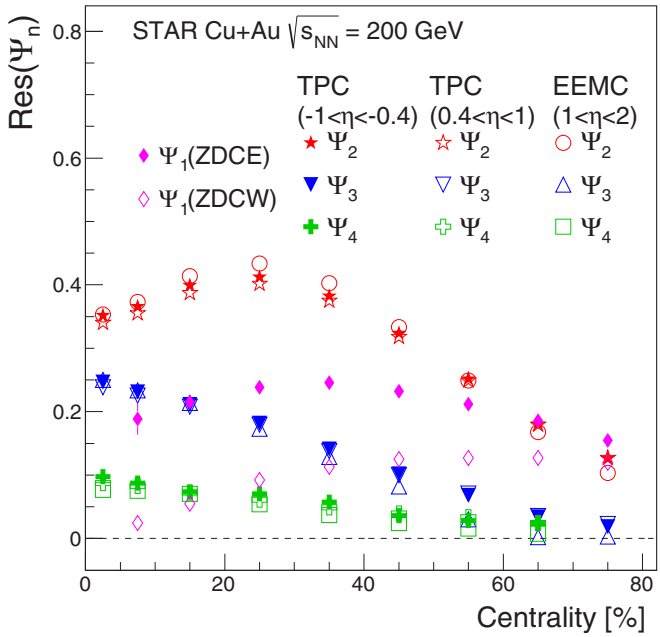

FIG. 3. Event plane resolutions as a function of centrality in Cu+Au collisions at $\sqrt{s_{NN}} = 200$ GeV.

x or y directions and sandwiched between the ZDC modules. Therefore, the SMD measures the centroid of the hadronic shower caused by the interaction between spectator neutrons and the ZDC. The x and y positions of the shower centroid was calculated for each ZDC-SMD on the event-by-event basis as follows:

$$\langle X \rangle = \frac{\sum_i X_i w_{X_i}}{\sum_i w_{X_i}}, \tag{7}$$

$$\langle Y \rangle = \frac{\sum_i Y_i w_{Y_i}}{\sum_i w_{Y_i}}, \tag{8}$$

where $X_i(Y_i)$ denotes the position of a vertical (horizontal) scintillator strip in the SMD and $w_{X_i}(w_{Y_i})$ denotes the ADC signal measured in each strip. Then the first-order event plane was determined as $\Psi_1 = \tan^{-1}(\langle Y \rangle / \langle X \rangle)$. The angle determined by the target spectators points into the opposite direction $(+\pi)$ to that of the projectile spectator plane, then the combined event plane of ZDC-SMD east and west can be obtained by summing Eqs. (7) and (8) from each ZDC-SMDs flipping the sign for one of them.

The event plane resolution defined as $\mathrm{Res}(\Psi_n) = \langle \cos(\Psi_n - \Psi_n^{\mathrm{obs}}) \rangle$ was estimated by the three-subevent method [44]. Here Ψ_n^{obs} denotes the azimuthal angle of a measured ("observed") event plane. For the first-order event plane, either BBC in the west (BBCW) or east (BBCE) sides was used as a third subevent along with the two ZDCs. For a higher harmonic event plane, three subevents from TPC were used. In the case of using the EEMC, one of the TPC subevents was replaced with EEMC subevent. In Au+Au collisions, both the two-subevent and the three-subevent methods were used. The results are reported using the reaction plane resolution from the two-subevent method, with the difference in results between the two methods included in the systematic uncertainty. Figure 3 shows the estimated event plane resolution, $\mathrm{Res}(\Psi_n) = \langle \cos(\Psi_n - \Psi_n^{\mathrm{obs}}) \rangle$ $(2 \leqslant n \leqslant 4)$, for TPC and EEMC, and $\mathrm{Res}(\Psi_1)$ for ZDC-SMD in Cu+Au collisions. Note that the forward direction or the west side (ZDCW and BBCW) is the Cu-going direction. The resolution of Ψ_1 with ZDC-SMD in Au+Au collisions can be found in Ref. [45]. Results for wide centrality bins in this study were obtained by taking averages of results measured with 10% step centrality bins.

C. Flow measurements

Azimuthal anisotropy was measured with the event plane method using the following equation:

$$v_n = \frac{\langle \cos[n(\phi - \Psi_n^{\mathrm{obs}})] \rangle}{\mathrm{Res}(\Psi_n)}, \tag{9}$$

where $\langle\,\rangle$ means an average over particles in an event, followed by the averaging over all events. We study v_n as a function of p_T for different centralities, as well as the (pseudo)rapidity dependence of v_1. For the event plane determined by TPC, the v_n of charged particles were measured using an η gap of 0.4 from the subevent used for the event plane determination, i.e., particles of interest were taken from $-1 < \eta < 0$ $(0 < \eta < 1)$ when using the event plane determined in the subevent from the forward (backward) rapidity. The results from these two subevents are found to be consistent and the average of the two measurements is used as the final result.

Directed flow can be also measured by the three-point correlator with the use of the second harmonic event plane [27]:

$$v_1\{3\} = \frac{\langle \cos(\phi + \Psi_1^{\mathrm{obs}} - 2\Psi_2^{\mathrm{obs}}) \rangle}{\mathrm{Res}(\Psi_1) \times \mathrm{Res}(\Psi_2)}, \tag{10}$$

where Ψ_1^{obs} and Ψ_2^{obs} were taken from different subevents and ϕ is the azimuthal angle of particles of interest in the rapidity region different from those subevents to avoid self-correlation. In our analysis, Ψ_1^{obs} was taken from the east BBC and Ψ_2^{obs} from either the TPC or EEMC subevents. The results for $v_1\{3\}$ obtained with TPC subevents from the backward and forward rapidities are statistically consistent in the overlapping region, and were further combined to cover the same η range for particles of interest as used in the event plane method. The difference between results obtained from TPC or EEMC subevents was taken into account as a systematic uncertainty. Note that Eq. (10) was calculated without any spectator information, and thus provides information on the directed flow projected onto the second harmonic participant plane.

For the higher harmonic flow measurements, the scalar product method [46–48] was tested for comparison with the event plane method. The scalar product method is equivalent to the two-particle correlation method with corresponding η gap between two particles and particle of interest. Three subevents were used to calculate the flow coefficients based on the following equation:

$$v_n = \frac{\langle \boldsymbol{u} \cdot \boldsymbol{Q}_n^A / N^A \rangle}{\sqrt{\frac{\langle \boldsymbol{Q}_n^B / N^B \cdot \boldsymbol{Q}_n^C / N^C \rangle}{\langle \boldsymbol{Q}_n^A / N^A \cdot \boldsymbol{Q}_n^B / N^B \rangle \langle \boldsymbol{Q}_n^C / N^C \cdot \boldsymbol{Q}_n^A / N^A \rangle}}}, \tag{11}$$

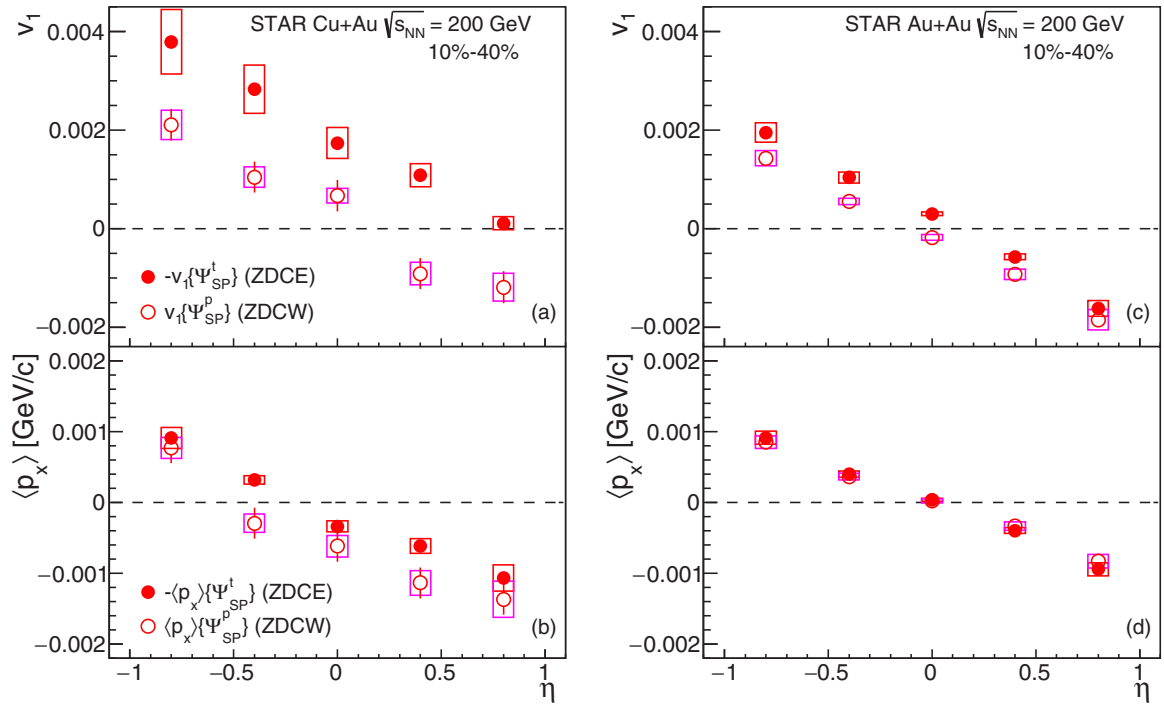

FIG. 4. Directed flow of charged particles measured with respect to the target (ZDCE) and projectile (ZDCW) spectator planes and the mean transverse momentum projected onto the spectator planes, as a function of η for $0.15 < p_T < 5\,\mathrm{GeV}/c$ in 10–40% centrality for Cu+Au (a),(b) and Au+Au (c),(d) collisions at $\sqrt{s_{NN}} = 200$ GeV. Open boxes show the systematic uncertainties. Note that the directed flow obtained with the target spectator plane ($v_1\{\Psi^t_{SP}\}$) is shown with opposite sign.

where $\boldsymbol{Q}_n$ is the flow vector defined in Eqs. (5) and (6) and the superscripts A, B, and C denote different subevents with a finite rapidity gap from the other subevent. The subevents were taken from TPC and/or EEMC. We denote by $\boldsymbol{u}$ a unit vector in the direction of the particle transverse momentum; N denotes the sum of weights used for reconstructing the flow vectors in each subevent.

The tracking efficiency was accounted for in p_T-integrated observables, although the effect of that is much smaller than other systematic uncertainties discussed below.

D. Systematic uncertainties

The systematic uncertainties were estimated by varying the track quality cuts described in Sec. III A and by varying collision z-vertex cut. The effect of the track quality cuts becomes largest at low p_T in central collisions and was found to be <4% for v_2, <6% for v_3, and <8% for v_4. The effect of the z-vertex cut is <1%. For identified particles, the effect of particle identification purity was also considered. The effect for charged pions is <1% in v_2 and v_3 and <3% in v_4. The effects for charged kaons and (anti)protons are <3% in v_2, <5% in v_3, and <10% in v_4. The combined estimated uncertainty was found to be p_T uncorrelated; namely all data points do not move in the same direction over p_T, and it was assigned as a point-by-point systematic uncertainty.

Along with the TPC event plane, the event plane determined by the EEMC was used for the v_n ($n \geqslant 2$) measurements and the difference in v_n obtained with the two methods was included in the systematic uncertainty. The latter was found to be p_T correlated: it was <2% (<10%) for v_2 and v_3 (v_4) in central collisions, and increased up to ∼5% (16%) for v_2 (v_3 and v_4) in peripheral collisions. For v_1, the details of the systematic uncertainty estimation can be found in our previous study [11]. As mentioned before, $v_1\{3\}$ was measured without the spectator information, but one can also use the ZDCs for Ψ_1 in Eq. (10) for a cross-check. We found that $v_1\{3\}$ measured using the ZDCs was consistent with $v_1\{3\}$ measured using the BBC within the uncertainties.

IV. DIRECTED FLOW

A. Directed flow of unidentified hadrons

The top panels, (a) and (c), of Fig. 4 present the directed flow v_1 of charged particles as a function of the pseudorapidity with respect to the target and projectile spectator planes in Cu+Au and Au+Au collisions at $\sqrt{s_{NN}} = 200$ GeV. It is taken into account that the projectile spectators deflect on average along the impact parameter vector (a vector from the center of the target to the center of the projectile, taken in this analysis to be Cu nucleus) [10]. The sign of v_1 measured with respect to the target spectator plane has been reversed. In both systems, a finite difference can be seen between v_1 measured with respect to each spectator plane. This indicates the existence of a fluctuation component (rapidity-even for symmetric collisions) of v_1 in both symmetric and asymmetric collision systems.

The notion of "odd" and "even" v_1 components can be justified only for symmetric collisions. Therefore, the following

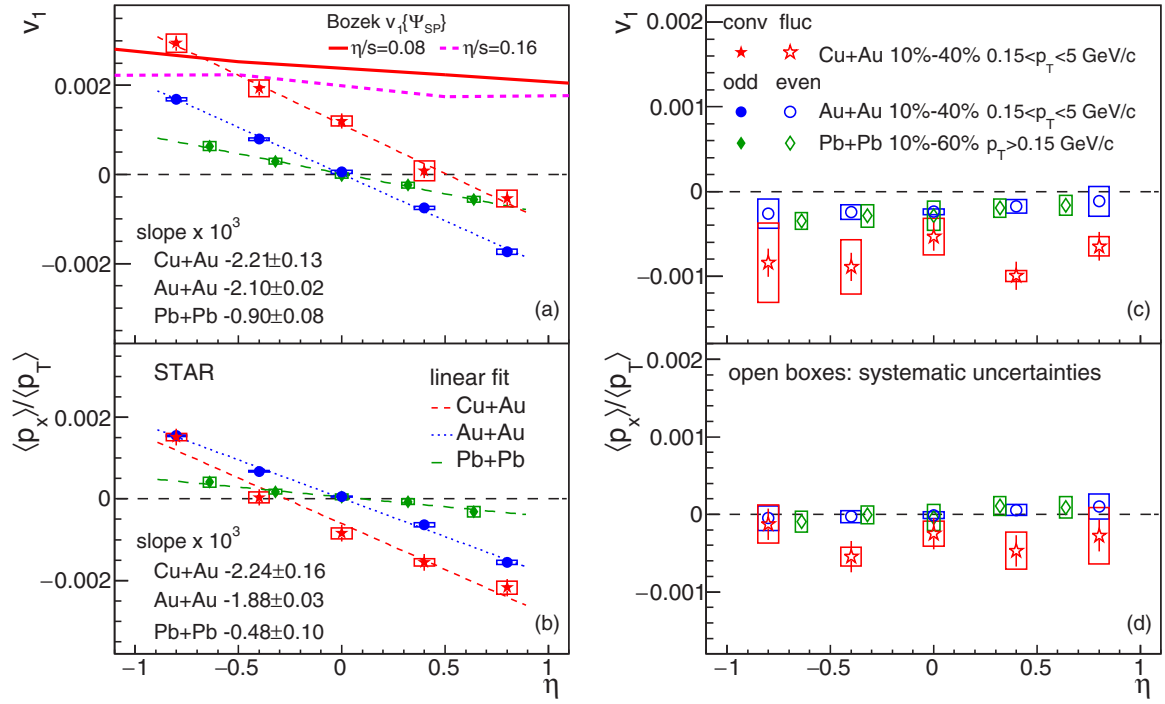

FIG. 5. Charged particle "conventional" (left) and "fluctuation" (right) components of directed flow v_1 and momentum shift $\langle p_x \rangle / \langle p_T \rangle$ as a function of η in 10–40% centrality for Cu+Au and Au+Au collisions at $\sqrt{s_{NN}} = 200$ GeV, and Pb+Pb collisions at $\sqrt{s_{NN}} = 2.76$ TeV [24]. Thick solid and dashed lines show the hydrodynamic model calculations with $\eta/s = 0.08$ and 0.16, respectively, for Cu+Au collisions [49]. Thin lines in the left panel show a linear fit to the data. Open boxes represent systematic uncertainties.

definitions are used for Cu+Au collisions:

$$v_1^{\mathrm{conv}} = \left(v_1\{\Psi_{\mathrm{SP}}^{p}\} - v_1\{\Psi_{\mathrm{SP}}^{t}\}\right)/2, \tag{12}$$

$$v_1^{\mathrm{fluc}} = \left(v_1\{\Psi_{\mathrm{SP}}^{p}\} + v_1\{\Psi_{\mathrm{SP}}^{t}\}\right)/2, \tag{13}$$

where "projectile" (Cu) spectators go into the forward direction. The term v_1^{conv} and v_1^{fluc} denotes "conventional" and "fluctuation" components of directed flow, respectively. Note that the right-hand side of Eqs. (12) and (13) represents the same definitions as Eqs. (2) and (3).

The mean transverse momentum projected onto the spectator plane defined as

$$\langle p_x \rangle = \frac{\langle p_T \cos\left(\phi - \Psi_1^{\mathrm{obs}}\right)\rangle}{\mathrm{Res}(\Psi_1)} \tag{14}$$

is also shown in the bottom panels, (b) and (d), of Fig. 4. There seems to be a small difference between results with two spectator planes in Cu+Au but not in Au+Au. The terms "conv (odd)" and "fluc (even)" are also used for $\langle p_x \rangle$ in the following discussion, with analogous definitions to Eqs. (12) and (13).

The top panels of Fig. 5 present the pseudorapidity dependence of $v_1^{\mathrm{odd(conv)}}$ and $v_1^{\mathrm{even(fluc)}}$, defined according to Eqs. (2), (3), (12), and (13). The $\langle p_x \rangle$ normalized by the mean p_T is also shown in the bottom panels. The lines represent linear fits to guide the eye. The conventional component of directed flow, v_1^{conv}, in Cu+Au has a similar slope to v_1^{odd} in Au+Au, with the intercept shifted to the forward direction. The mean transverse momentum component $\langle p_x^{\mathrm{conv}} \rangle$ in Cu+Au might deviate from linear dependence (observed in Au+Au) with the slope slightly increasing at backward rapidities. This trend in $\langle p_x^{\mathrm{conv}} \rangle$ might reflect the momentum balance between particles produced in the forward and backward hemispheres—in Cu+Au collisions more charged particles are produced in the Au-going direction, and therefore the particles at forward rapidity need to have a larger p_x on average to compensate for the asymmetric multiplicity distribution over η. Results from Pb+Pb collisions at $\sqrt{s_{NN}} = 2.76$ TeV measured by the ALICE experiment [24] are also shown in Fig. 5. The slope of v_1^{odd} in Pb+Pb collisions is about three times smaller than that in Au+Au collisions. This trend, i.e., the energy dependence of the v_1 slope, is consistent with that observed in the RHIC beam energy scan [50]. Calculations from an event-by-event hydrodynamic model with two different values of η/s ($\eta/s = 0.08$ and 0.16) for Cu+Au collisions [49] are also compared to the data. Despite the model's successful description of elliptic flow and triangular flow (see Sec. V), it cannot reproduce either the magnitude of the directed flow nor its pseudorapidity dependence.

The even component of directed flow, v_1^{even}, in Au+Au does [Fig. 5(c)] not depend on pseudorapidity (within error bars) and is very similar in magnitude to v_1^{even} in Pb+Pb collision at LHC energies. The $\langle p_x^{\mathrm{even}} \rangle$ in both Au+Au and Pb+Pb collisions is consistent with zero, which indicates zero net transverse momentum in the systems. This agrees with the expectation that the even component of v_1 originates from event-by-event fluctuations of the initial density. The magnitude of v_1^{fluc} in Cu+Au is larger than that of v_1^{even} in Au+Au. This would be due either to larger initial density fluctuations in Cu+Au collisions or to stronger correlations between the spectator and dipole fluctuation planes.

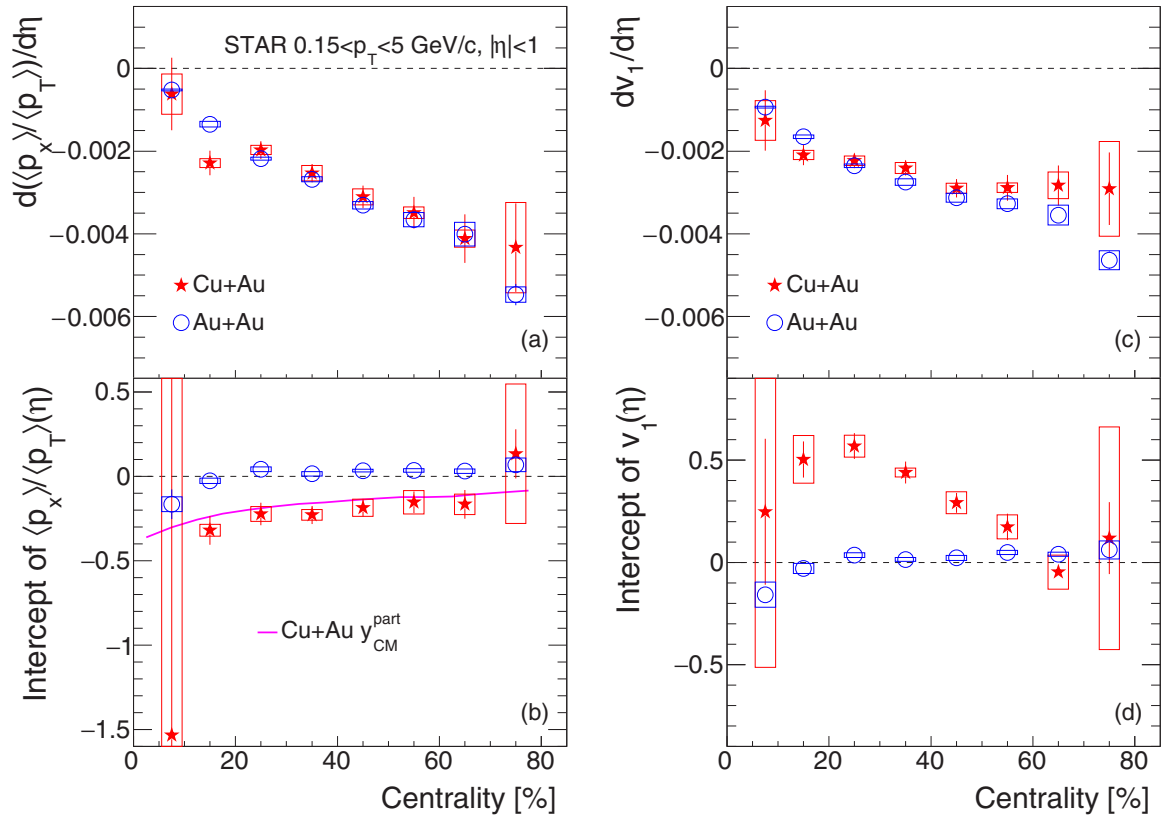

FIG. 6. Slopes and intercepts of $\langle p_x\rangle/\langle p_T\rangle(\eta)$ and $v_1(\eta)$ as a function of centrality in Cu+Au and Au+Au collisions at $\sqrt{s_{NN}} = 200$ GeV. The solid line shows the center-of-mass rapidity in Cu+Au collisions calculated by Cu and Au participants in a Glauber model. Open boxes represent systematic uncertainties.

The results presented in Figs. 4 and 5, and in particular a positive intercept of $v_1(\eta)$ and negative intercept of $\langle p_x\rangle$, are consistent with a picture of directed flow in Cu+Au collisions as a superposition of that from a "tilted source" (shifted in rapidity to the system center-of-mass rapidity) and dipole flow due to nonzero average density gradients. Compared to the $v_1(\eta)$ dependence in symmetric collisions, the first mechanism shifts the function toward negative rapidities, and the second moves the entire function up (note that the Cu nucleus is defined as the projectile) as shown in Figs. 1(a) and 1(b). This picture receives further support from the study of the centrality dependence of the corresponding slopes and intercepts presented in Fig. 6. Very similar slopes of v_1 and $\langle p_x\rangle/\langle p_T\rangle$ would be a natural consequence of a tilted source. The intercepts of $\langle p_x\rangle$ follow very closely the shift in rapidity center of mass of the system shown with the solid line in Fig. 6(b), which was calculated by a Monte Carlo Glauber model based on the ratio of Au and Cu participant nucleons:

$$y_{\rm CM} \approx \tfrac{1}{2}\ln\left(N_{\rm part}^{\rm Au}/N_{\rm part}^{\rm Cu}\right), \tag{15}$$

where $N_{\rm part}^{\rm Au(Cu)}$ is the number of participants from Au or Cu nuclei. The centrality dependence of v_1 intercept (more exactly, in this picture the difference in v_1 and $\langle p_x\rangle$ intercepts) in Fig. 6(d) would be mostly determined by the decorrelations between the dipole flow direction $\Psi_{1,3}$ and the reaction (spectator) planes.

The slopes of $v_1^{\rm odd(conv)}$ and $\langle p_x^{\rm conv}\rangle/\langle p_T\rangle$ in Fig. 5 agree within 10% both in Au+Au and Cu+Au collisions. In Pb+Pb collisions at the LHC energy the v_1 slope is almost a factor of 2 larger in magnitude than that of $\langle p_x^{\rm conv}\rangle/\langle p_T\rangle$. This clearly indicates that both mechanisms, tilted source (for which one would expect the slope of $\langle p_x^{\rm conv}\rangle/\langle p_T\rangle$ to be about 50% larger than that of $v_1^{\rm odd(conv)}$; see the Appendix) and initial density asymmetries (for which $\langle p_x^{\rm conv}\rangle = 0$), play a significant role in the formation of the directed flow even in symmetric collisions. The relative contribution of the tilted source mechanism to the v_1 slope r can be expressed as (see the Appendix)

$$r = \frac{\left(\frac{dv_1}{d\eta}\right)^{\rm tilt}}{\frac{dv_1}{d\eta}} \approx \frac{2}{3}\frac{\frac{1}{\langle p_T\rangle}\frac{d\langle p_x\rangle}{d\eta}}{\frac{dv_1}{d\eta}}, \tag{16}$$

where $()^{\rm tilt}$ denotes a contribution from the tilted source. The relative contribution r is about 2/3 at the top RHIC collision energies decreasing to about 1/3 at LHC energies. From the centrality dependence of slopes shown in Fig. 6 one can conclude that the relative contribution of the tilted source mechanism is largest in peripheral collisions (where the $\langle p_x^{\rm conv}\rangle/\langle p_T\rangle$ slope is approximately 1.5 times larger than that of $v_1^{\rm odd(conv)}$) and smallest in central collisions. This dependence might be due to the stronger decorrelation between spectator and dipole flow planes in peripheral collisions. Figure 7 shows the even (fluctuation) components of v_1 and $\langle p_x\rangle$ as a function of centrality. The $v_1^{\rm even}$ for Au+Au has a weak centrality dependence and is consistent with $v_1^{\rm even}$ for Pb+Pb except in most peripheral collisions. Furthermore, $p_x^{\rm even}$ in both Au+Au

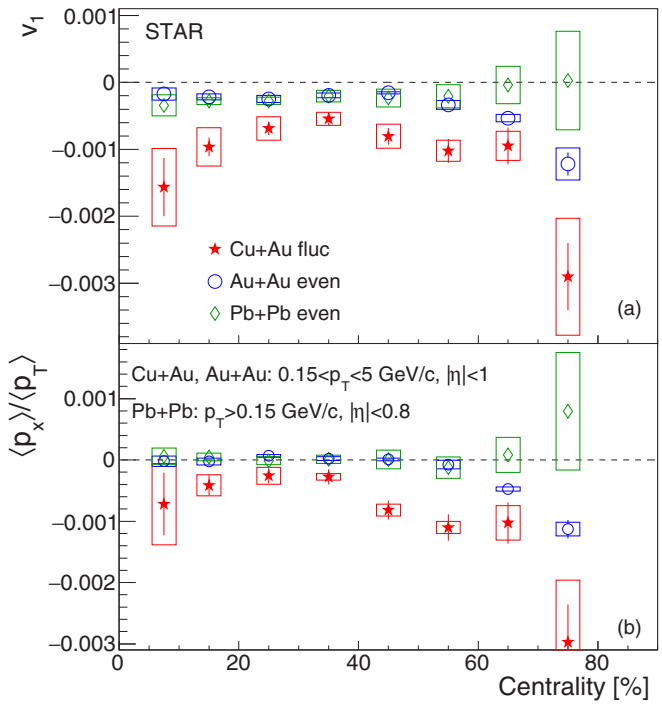

FIG. 7. Centrality dependence of the even (fluctuation) components of v_1 and $\langle p_x \rangle / \langle p_T \rangle$ in Cu+Au and Au+Au collisions at $\sqrt{s_{NN}} =$ 200 GeV and Pb+Pb collisions at $\sqrt{s_{NN}} = 2.76$ TeV [24]. Open boxes represent systematic uncertainties.

and Pb+Pb are consistent with zero. This may indicate that the dipolelike fluctuation in the initial state has little dependence on the system size and collision energy. $v_1^{\rm fluc}$ and $\langle p_x \rangle^{\rm fluc}$ for Cu+Au has a larger magnitude than in symmetric collisions over the entire centrality range; it is smallest in the 30–40% centrality bin.

The reference angle of dipole flow can be represented by $\Psi_{1,3}$, but $v_1^{\rm even}$ ($v_1^{\rm fluc}$) are the projections of dipole flow onto the spectator planes. Therefore, the measured even (or fluctuation) components of v_1 should be decreased by a factor $\langle \cos(\Psi_{1,3} - \Psi_{\rm SP}) \rangle$. Such a "resolution" effect may also lead to larger $v_1^{\rm even}$ and nonzero $\langle p_x^{\rm even} \rangle$ in Cu+Au collisions due to the difference in correlation of the Cu and Au spectator planes to $\Psi_{1,3}$.

The p_T dependence of $v_1^{\rm conv}$ and $v_1^{\rm fluc}$ in Cu+Au collisions was studied for different collision centralities, as shown in Fig. 8. The $v_1^{\rm conv}$ exhibits a sign change around $p_T = 1$ GeV/c and its magnitude at both low and high p_T becomes smaller for peripheral collisions. Such centrality dependence in Cu+Au $v_1^{\rm conv}$ can be due to a change in the correlation between the angle of the initial density asymmetry and the direction of spectator deflection. The correlation becomes largest at an impact parameter of 5 fm (which corresponds approximately to 10–20% centrality) and decreases in more peripheral collisions as discussed in Ref. [10]. Similar p_T and centrality dependencies were observed in $v_1^{\rm fluc}$ although there is a difference in sign between $v_1^{\rm conv}$ and $v_1^{\rm fluc}$. An event-by-event viscous hydrodynamic model calculation is also compared to the $v_1^{\rm conv}$ for the 20–30% centrality bin in Cu+Au collisions. As seen in Fig. 8, the model qualitatively follows the shape of the measurement but overpredicts the data in its magnitude for the entire p_T region.

The odd and even components of directed flow, $v_1^{\rm odd}$ and $v_1^{\rm even}$, in Au+Au collisions are also compared in the same

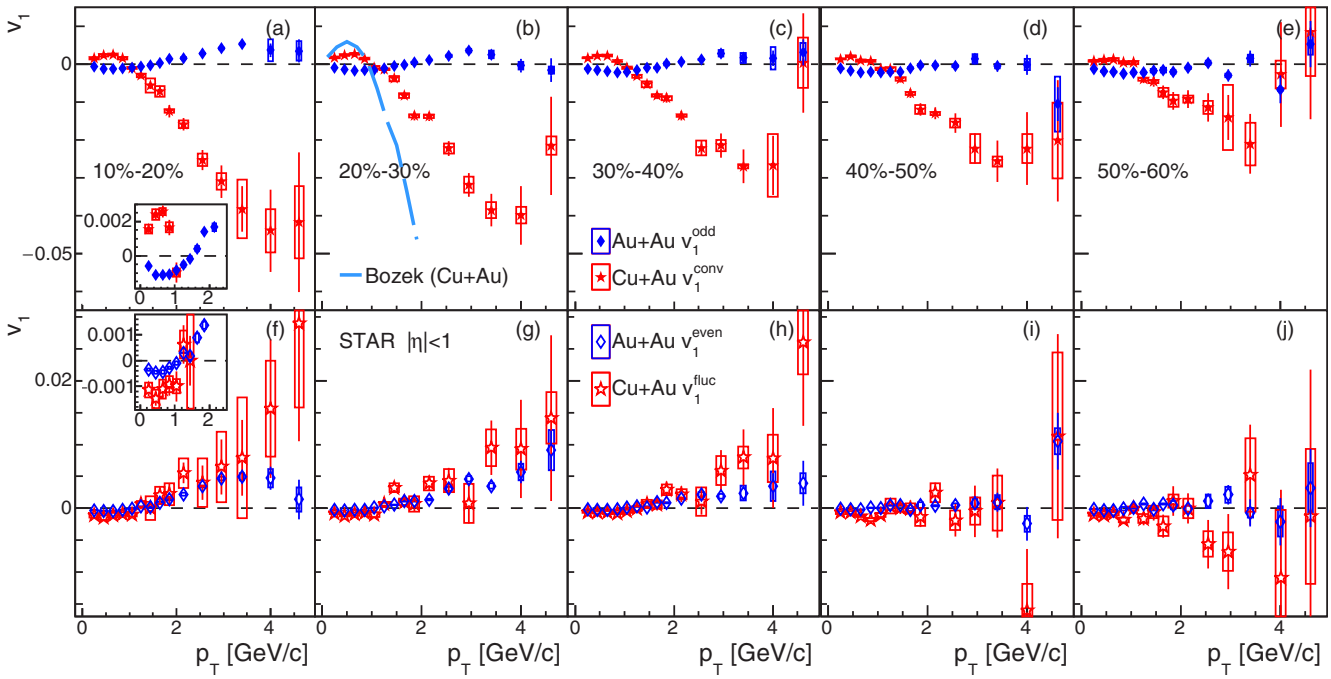

FIG. 8. The conventional (a)–(e) and fluctuation (f)–(j) components of directed flow, $v_1^{\rm conv(odd)}$ and $v_1^{\rm fluc(even)}$, of charged particles as a function of p_T for different collision centralities in Cu+Au and Au+Au collisions. Open boxes represent systematic uncertainties. The broken line in panel (b) shows the viscous hydrodynamic calculation for Cu+Au collisions [49].

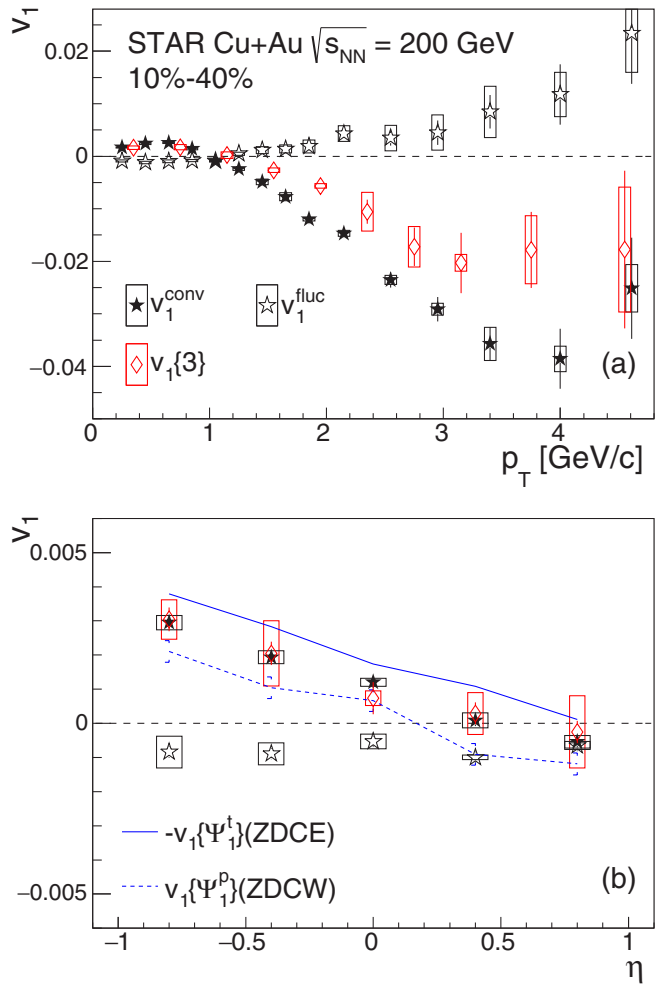

FIG. 9. Directed flow of charged particles as a function of p_T (a) and η (b) in the 10–40% centrality bin measured with the ZDC-SMD event planes and three-point correlator in Cu+Au collisions. The p_T dependence was measured in $|\eta| < 1$ and the η dependence was integrated over $0.15 < p_T < 5$ GeV/c. Open boxes represent systematic uncertainties.

centrality windows, where v_1^{odd} was measured by flipping the sign for particles with the negative rapidity. The signals of both v_1^{odd} and v_1^{even} in Au+Au are smaller than directed flow in Cu+Au but, at least in central collisions, they still show the sign change in the p_T dependence.

The v_1 with the three-point correlator, $v_1\{3\}$, was measured in Cu+Au collisions for the 10–40% centrality bin as shown in Fig. 9, where it is compared to v_1^{conv} and v_1^{fluc} from the event plane method using spectator planes. Note that $v_1\{3\}$ does not use spectator information. The $v_1\{3\}$ is consistent with v_1^{conv} for $p_T < 1$ GeV/c within the systematic uncertainties but becomes greater than v_1^{conv} for $1 < p_T < 4$ GeV/c. The $v_1\{3\}$ includes both conventional and fluctuation components of v_1. The conventional component in $v_1\{3\}$ should be the same as measured by the event plane method but the fluctuation component might be different due to different correlations of the spectator planes and participant plane (from the BBC subevent) with $\Psi_{1,3}$.

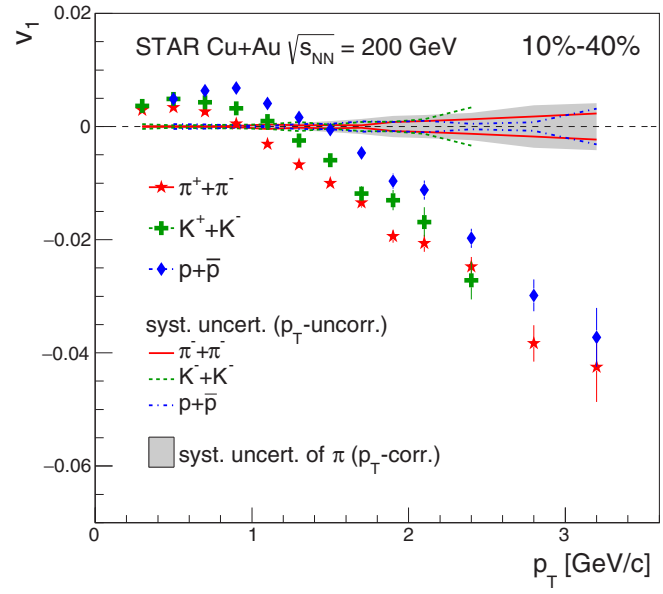

FIG. 10. Directed flow of $\pi^+ + \pi^-$, $K^+ + K^-$, and $p + \bar{p}$ as a function of p_T for $|\eta| < 1$ in the 10–40% centrality bin. The p_T-uncorrelated systematic uncertainties are shown with lines around $v_1 = 0$ for each particle species. p_T-correlated systematic uncertainty is shown only for pions with a shaded band.

B. Directed flow of identified hadrons

Anisotropic flow of charged pions, kaons, and (anti)protons was measured based on the particle identification with the TPC and TOF, as explained in Sec. III A. Figure 10 presents directed flow of $\pi^+ + \pi^-$, $K^+ + K^-$, and $p + \bar{p}$ measured with respect

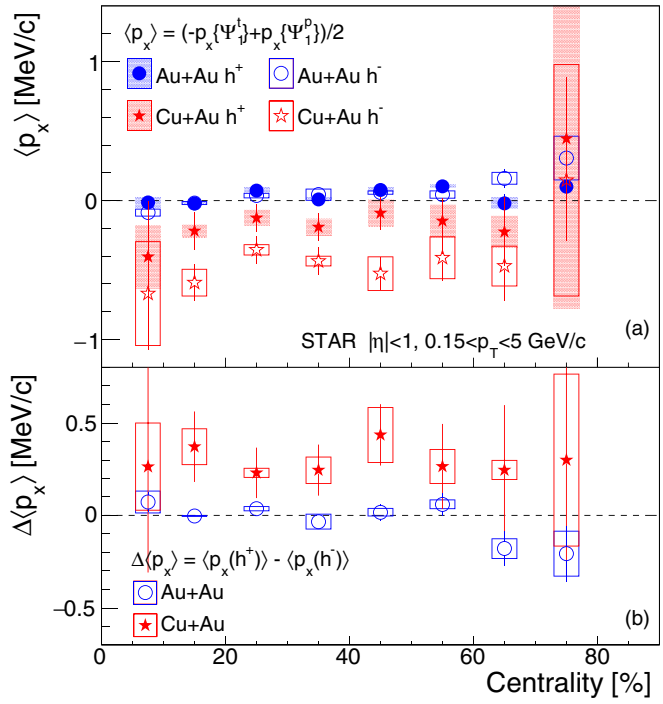

FIG. 11. Positively and negatively charged particles $\langle p_x \rangle$ and the difference $\Delta\langle p_x \rangle$ as a function of centrality in Au+Au and Cu+Au collisions. Open and shaded boxes show systematic uncertainties.

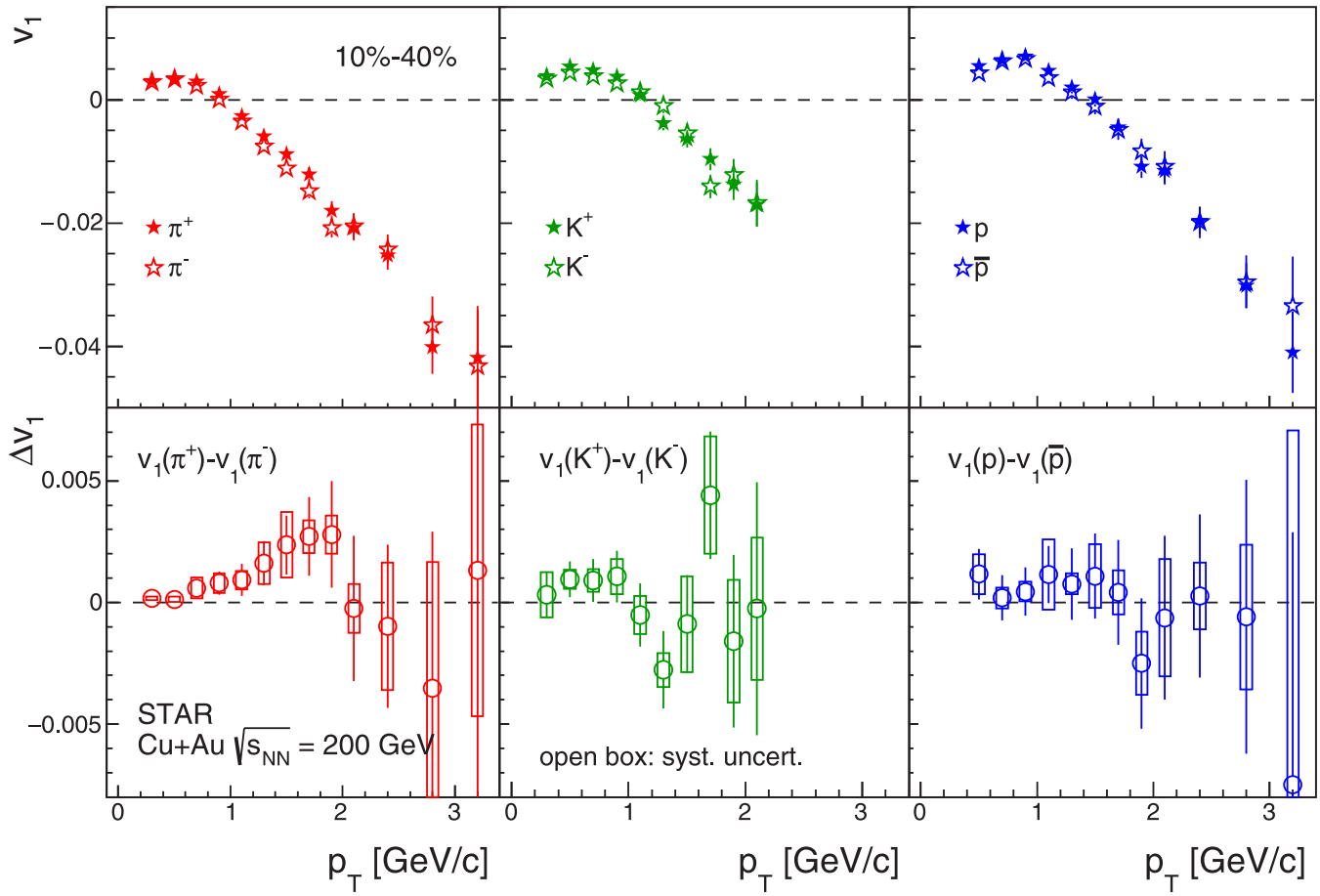

FIG. 12. Directed flow of π^+, π^-, K^+, K^-, p, and $\bar{p}$ measured in $|\eta| < 1$ as a function of p_T for the 10–40% centrality bin in Cu+Au collisions (top panels), where only the statistical uncertainties are shown. The differences in the directed flow between positively and negatively charged particles are shown in bottom panels, where the open boxes show the systematic uncertainties.

to the target (Au) spectator plane ($v_1 = -v_1\{\Psi_{\rm SP}^t\}$) in the 10–40% centrality bin. For $p_T < 2$ GeV/c, there is a clear particle type dependence, likely reflecting the effect of particle mass in interplay of the radial and directed flow [51,52]. In the $p_T > 2$ GeV/c region, there is no clear particle type dependence due to the large uncertainties. Measurement of identified particle v_1 with the projectile (Cu) spectator plane is difficult due to small statistics of identified particles and poor event plane resolution; therefore we do not decompose the v_1 into the conventional and fluctuation components. The presented v_1 of $\pi^+ + \pi^-$, $K^+ + K^-$, and $p + \bar{p}$ includes both components. The observed mass dependence in the v_1 of identified particles is consistent with results from the PHENIX Collaboration [53].

C. Charge dependence of directed flow

In our previous study [11], a finite difference in directed flow between positively and negatively charged particles was observed in asymmetric Cu+Au collisions. These results can be understood as an effect of the electric field due to the asymmetry in the electric charge of the Au and Cu nuclei. Similarly, one would expect a difference in $\langle p_x \rangle$ between positive and negative particles. Figure 11 shows the centrality dependence of charge-dependent $\langle p_x \rangle$ and the difference $\Delta\langle p_x \rangle$ between positive and negative particles in Au+Au and Cu+Au collisions. The difference is consistent with zero for Au+Au collisions, but a finite difference is observed in Cu+Au collisions ($\Delta\langle p_x \rangle \sim 0.3$ MeV/c). The direction of the electric field is expected to be strongly correlated to the direction of the Cu (projectile) spectator deflection, which should lead to a positive $\langle p_x \rangle$ by the convention used in this analysis. The results are consistent with these expectations.

The magnitude of the momentum shift can be roughly estimated based on the equation of motion, i.e., $\Delta p_x = e|\vec{E}|/m_\pi^2 \times m_\pi^2 \times \Delta t$ where $\vec{E}$ denotes the electric field, m_π is a pion mass, and Δt is the lifetime of the electric field. If one takes $e|\vec{E}|/m_\pi^2 \sim 0.9$ and $\Delta t \sim 0.1$ fm/c [9], assuming that the time dependence of the electric field approximates a step function, the resulting Δp_x is ~9 MeV/c which is ~30 times larger than the observed $\Delta\langle p_x \rangle$. The charge dependence of $\Delta\langle p_x \rangle$ is determined by the number of charges, i.e., the number of quarks and antiquarks, at the time when the initial electric field is strong after the collisions. Therefore a difference in $\Delta\langle p_x \rangle$ between the data and our estimate might indicate a smaller number of quarks and antiquarks at early times ($t < 0.1$ fm/c) compared to the number of quarks in the final state, as discussed in Ref. [11]. The lifetime of the electric field depends on the model and could be longer if the medium has a

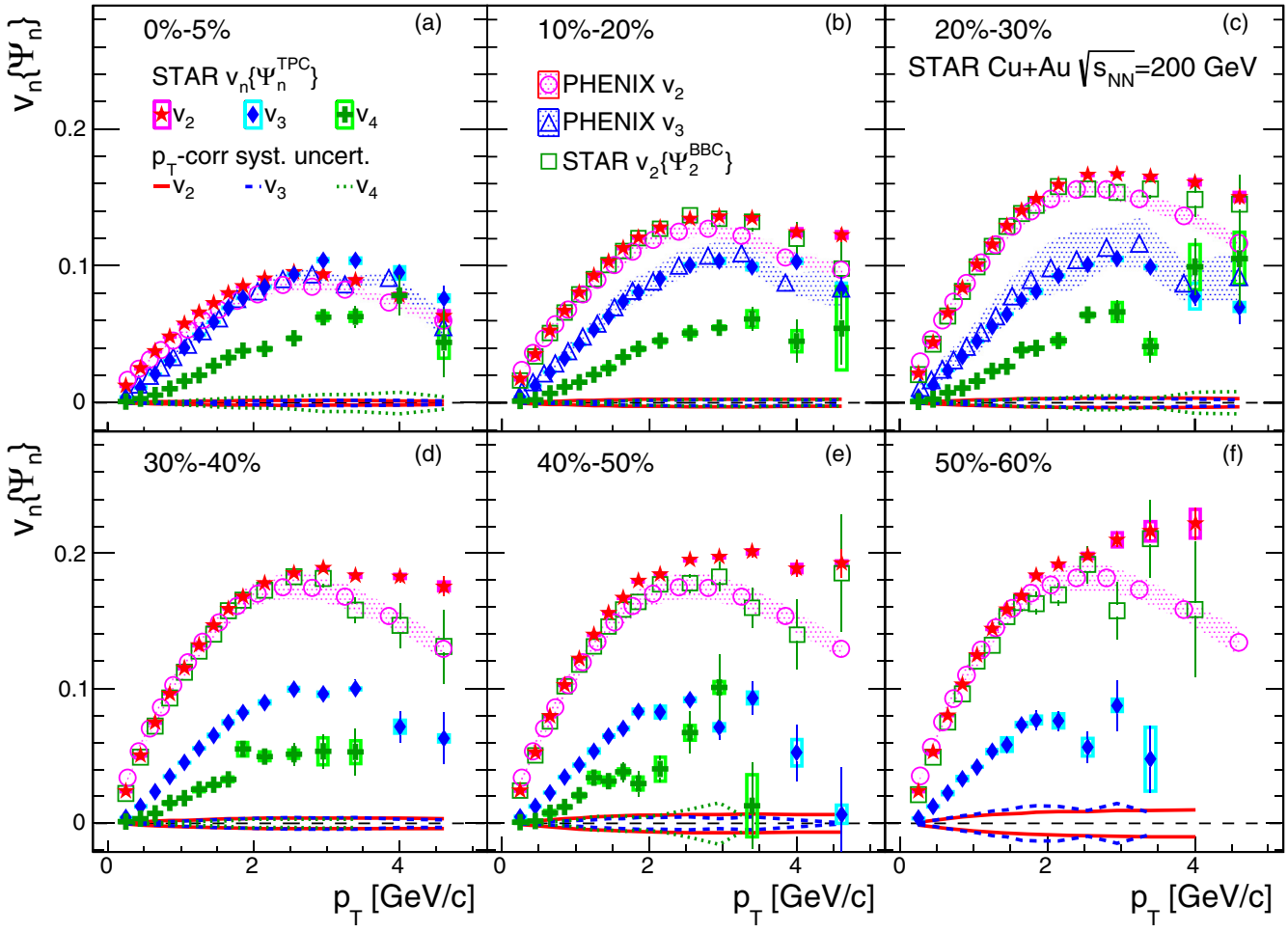

FIG. 13. Higher harmonic flow coefficients $v_n\{\Psi_n\}$ of charged particles in Cu+Au collisions as a function of p_T for six centrality bins. Colored boxes around the data points show p_T-uncorrelated systematic uncertainties and solid thin lines around $v_n = 0$ show p_T-correlated systematic uncertainties. Results from the PHENIX experiment [53] are compared. Only statistical uncertainty is shown for $v_2\{\Psi_2^{\mathrm{BBC}}\}$.

larger conductivity. Also note that the observed $\Delta\langle p_x\rangle$ might be smeared by the fluctuations between the direction of the electric field and the spectator plane, and by hydrodynamic evolution and hadron rescattering at later stages of the collisions.

For a mere detailed view of the quark-antiquark production dynamics, as well as to understand the role of baryon stopping in the development of directed flow at midrapidity, we also extended our measurements to identified particles. In the so-called "two-wave" scenario of quark production [54], the number of s quarks approximately remains the same during the system evolution while the number of u and d quarks sharply increases at the hadronization time. In this case, one might expect a relatively larger effect of the initial electric field for s quarks than for u and d quarks. Therefore the measurement of charge-dependent v_1 for pions and kaons might serve as a test of such a quark production scenario. The difference in number of protons and neutrons in the colliding nuclei in combination with the baryon stopping might also contribute to the charge dependence of directed flow. In this case one can expect a significantly larger effect measuring the flow of baryons itself. For that we measure the charge dependence of directed flow of protons and antiprotons.

The top panels in Fig. 12 show p_T dependence of v_1 separately for π^+ and π^-, K^+ and K^-, and p and $\bar{p}$ for 10–40% centrality in Cu+Au collisions. Bottom panels show difference in v_1, Δv_1, between positively and negatively charged particles for each species. Similarly as observed for charged hadrons [11] and in agreement with results presented in Fig. 11, v_1 of π^+ is larger than that of π^- in the $p_T < 2\ \mathrm{GeV}/c$ region, which is consistent with the expectation from the initial electric field effect. For charged kaons and (anti)protons, no significant differences are observed within the current experimental precision.

V. ELLIPTIC AND HIGHER HARMONIC FLOW

A. Unidentified charged particles

Higher harmonic anisotropic flow coefficients v_n of charged particles were measured with TPC η subevents as a function of p_T up to $n = 4$. Results for six centrality bins (0–5%, 10–20%, 20–30%, 30–40%, 40–50%, and 50–60%) are shown in Fig. 13. Results for v_2 and v_3 from the PHENIX experiment [53], shown for comparison, agree well with our results within uncertainties. The small difference in v_2 for $p_T > 2\ \mathrm{GeV}/c$

can be explained by a different contribution from nonflow correlations—PHENIX measured v_2 with a larger η gap ($\Delta\eta > 2.65$) between the particles of interest and those used for the event plane determination, while our TPC η subevents have $\Delta\eta > 0.4$. To confirm that explanation, we also calculated v_2 with respect to the BBC event plane, which ensures $\Delta\eta > 2.3$. Those results, while having larger statistical uncertainties, are consistent with the PHENIX measurements.

As with Au+Au collisions [5,27,55], the elliptic flow v_2 in Cu+Au collisions depends strongly on centrality, increasing significantly toward more peripheral collisions. The v_3 and v_4 have weak centrality dependencies. In the most central collisions, the magnitude of v_3 is comparable to, or even greater than, v_2 for $p_T > 2$ GeV/c. A similar trend has been observed at the LHC [56].

To make a comparison with Au+Au collisions, the Cu+Au results are plotted as a function of the number of participants for two different p_T bins in Fig. 14. Results for Au+Au collisions were taken from the previous studies by STAR [27,55] and PHENIX [5]. The elliptic flow v_2 has a strong centrality dependence in both systems due to the variation of the initial eccentricity, while v_3 and v_4 have much weaker centrality dependence reflecting their mostly fluctuation origin. The triangular flow v_3 as a function of the number of participants in Cu+Au falls on the same curve as in Au+Au. This suggests that v_3 (determined by the initial triangularity) is dominated by fluctuations, which are directly related to the number of participants. The v_4 in Au+Au is slightly larger than in Cu+Au. These relations between v_n in the two systems can be qualitatively explained by the initial spatial anisotropy ε_n [57]. A larger v_4 in Au+Au collisions compared to that in Cu+Au may be due to a larger v_2 and v_2-v_4 nonlinear coupling that cannot be fully accounted for by the ε_2-ε_4 correlation [58].

Hydrodynamic models have successfully described the azimuthal anisotropy measured in symmetric collisions. The comparison of the data to model calculations provided valuable constraints on the shear viscosity over entropy density η/s [4,5]. Further constraints can be obtained from a similar comparison for asymmetric collisions. Figure 15 compares v_2 and v_3 in Cu+Au collisions to the viscous hydrodynamic calculations [49]. The model employs the Glauber (participant nucleons) initial density distribution and applies the event-by-event viscous hydrodynamic model with $\eta/s = 0.08$ or 0.16. Both v_2 and v_3 are reasonably well described by the model at $p_T < 2$ GeV/c. The calculation with $\eta/s = 0.08$ seems to work better in the 0–5% centrality bin, while the 20–30% centrality results might need a larger η/s. In the same figure we also compare v_2 and v_3 measured with the scalar product method to the corresponding measurements obtained with the event plane method. Both methods use TPC η subevents. The results are in a very good agreement with each other.

Figure 16 compares our results to a multiphase transport (AMPT) model [59] (v1.26t5 for the default version and v2.26t5 for the string melting version). The initial conditions in this model are determined by the heavy ion jet interaction generator (HIJING) [60] which is based on the Glauber model and creates minijet partons and excited strings. In the AMPT default version, the strings are converted into hadrons via

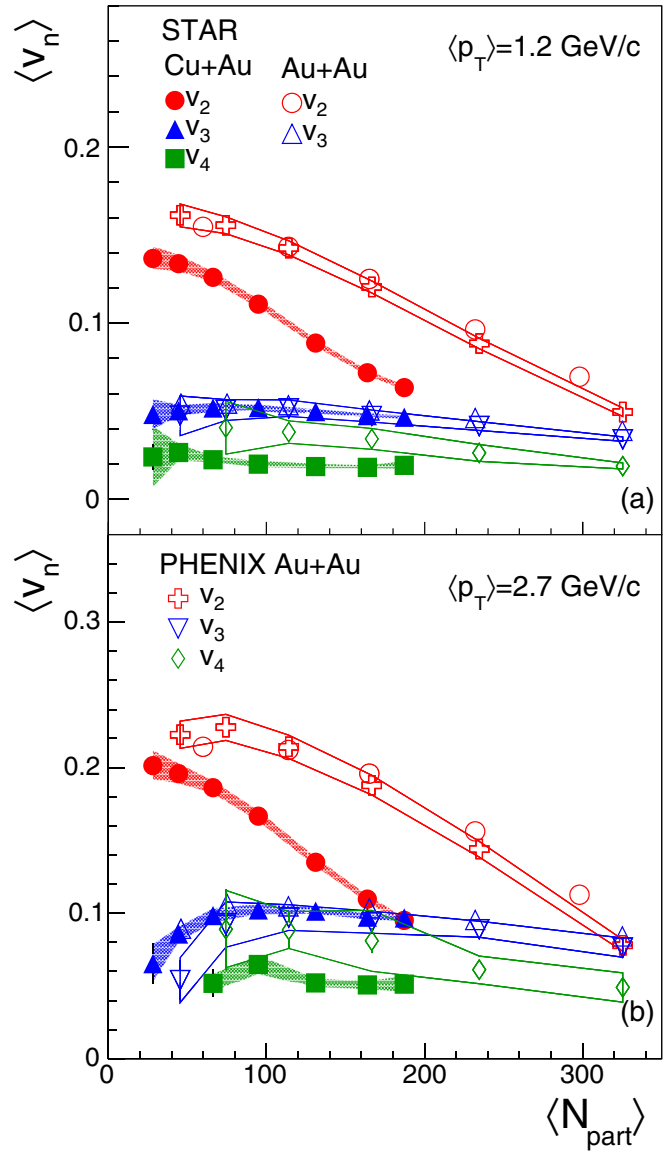

FIG. 14. Higher harmonic flow coefficients v_n of charged particles for two selected p_T bins as a function of the number of participants calculated with a Monte Carlo Glauber simulation for Cu+Au and Au+Au collisions, comparing with results in Au+Au from the PHENIX experiment [5]. Open and shaded bands represent systematic uncertainties.

string fragmentation, while in the string melting version the strings are first converted to partons (constituent quarks) and the created partons are converted to hadrons via a coalescence process after the subsequent parton scatterings.

The event plane and centrality in the model calculations were determined in the same way as in the real data analysis. Flow measurements were also performed in the same way. Figure 16 shows v_n for the 0–5%, 10–20%, and 30–40% centrality bins compared to the AMPT model in the default and string melting versions. The parton cross section in the string melting version was set to $\sigma_{\text{parton}} = 1.5$ mb [61,62]. The AMPT calculations with the default version and the string melting version with $\sigma_{\text{parton}} = 1.5$ mb qualitatively describe the data

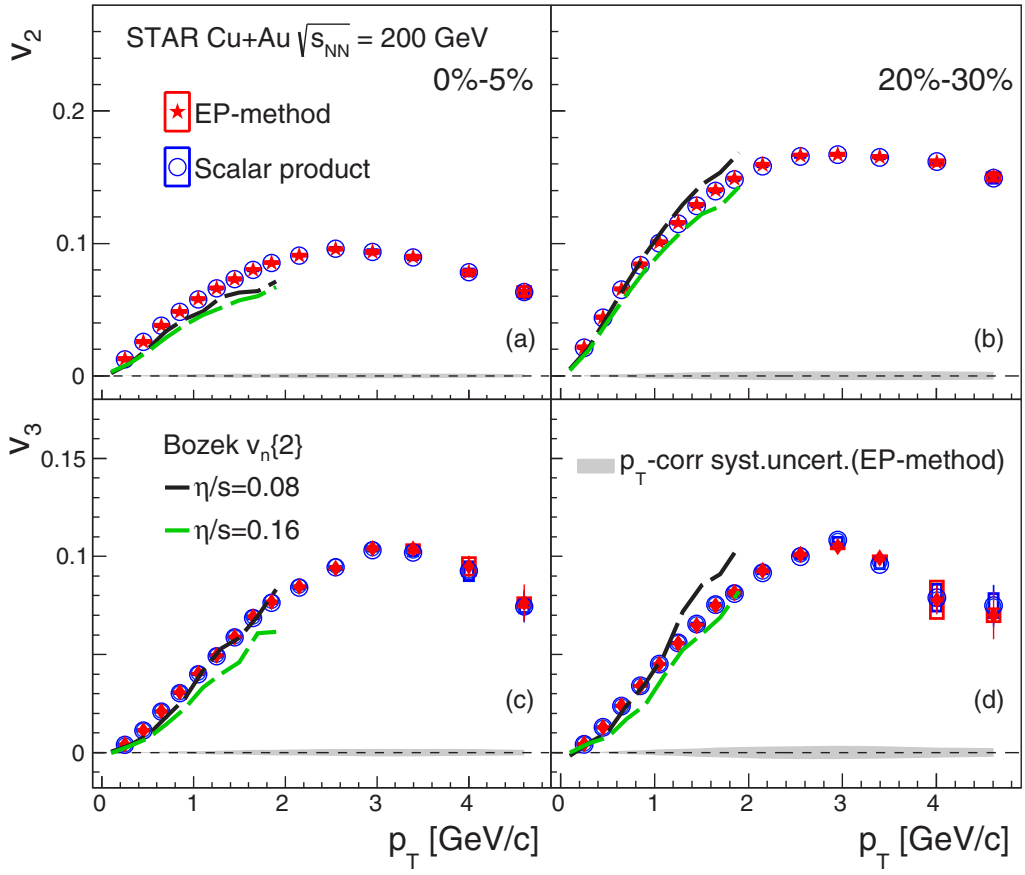

FIG. 15. The second and third harmonic flow coefficients of charged particles as a function of p_T measured with the event plane (EP) method and scalar product method, comparing to the viscous hydrodynamic calculations [49]. Panels (a) and (c) are for 0–5% centrality, panels (b) and (d) for 20–30% centrality.

of v_2, v_3, and v_4 for $p_T < 3$ GeV/c. The data are between the default and string melting with $\sigma_{\text{parton}} = 1.5$ mb results, similar to the observation in Refs. [37,62].

B. Flow of identified hadrons and NCQ scaling

Anisotropic flow of charged pions, kaons, and (anti)protons was also measured for higher harmonics ($n = 2$–4). Figure 17

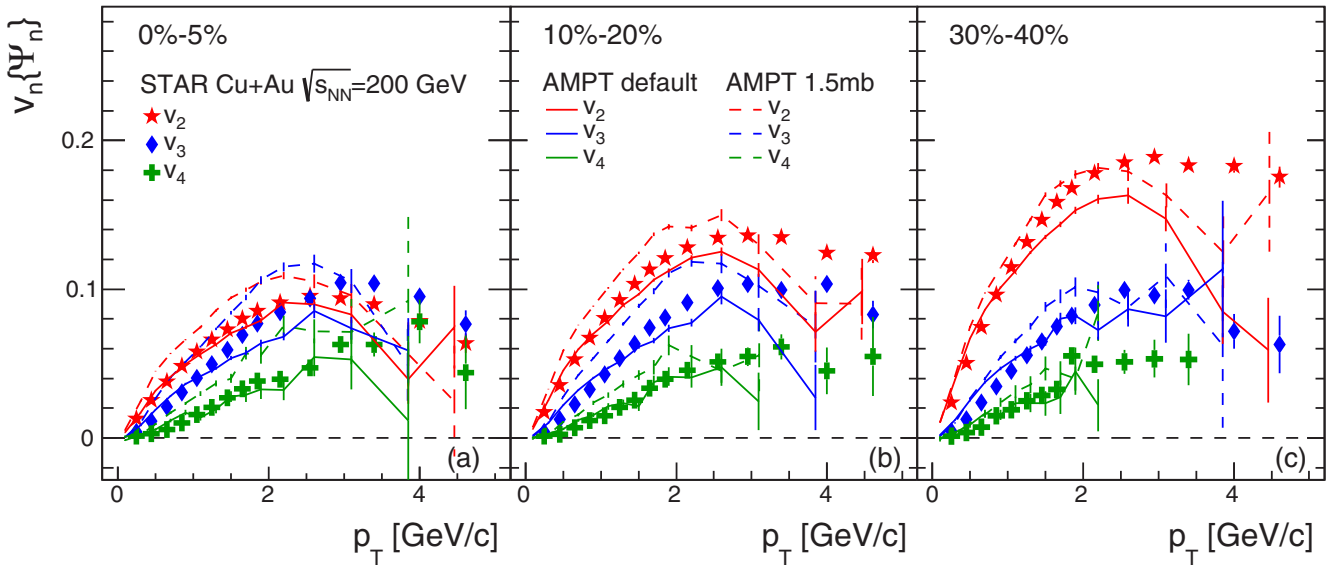

FIG. 16. Higher harmonic flow coefficients v_n of charged particles as a function of p_T comparing to the AMPT model [59], where solid lines are for default AMPT setup and dashed lines are for the string melting version with $\sigma_{\text{parton}} = 1.5$ mb.

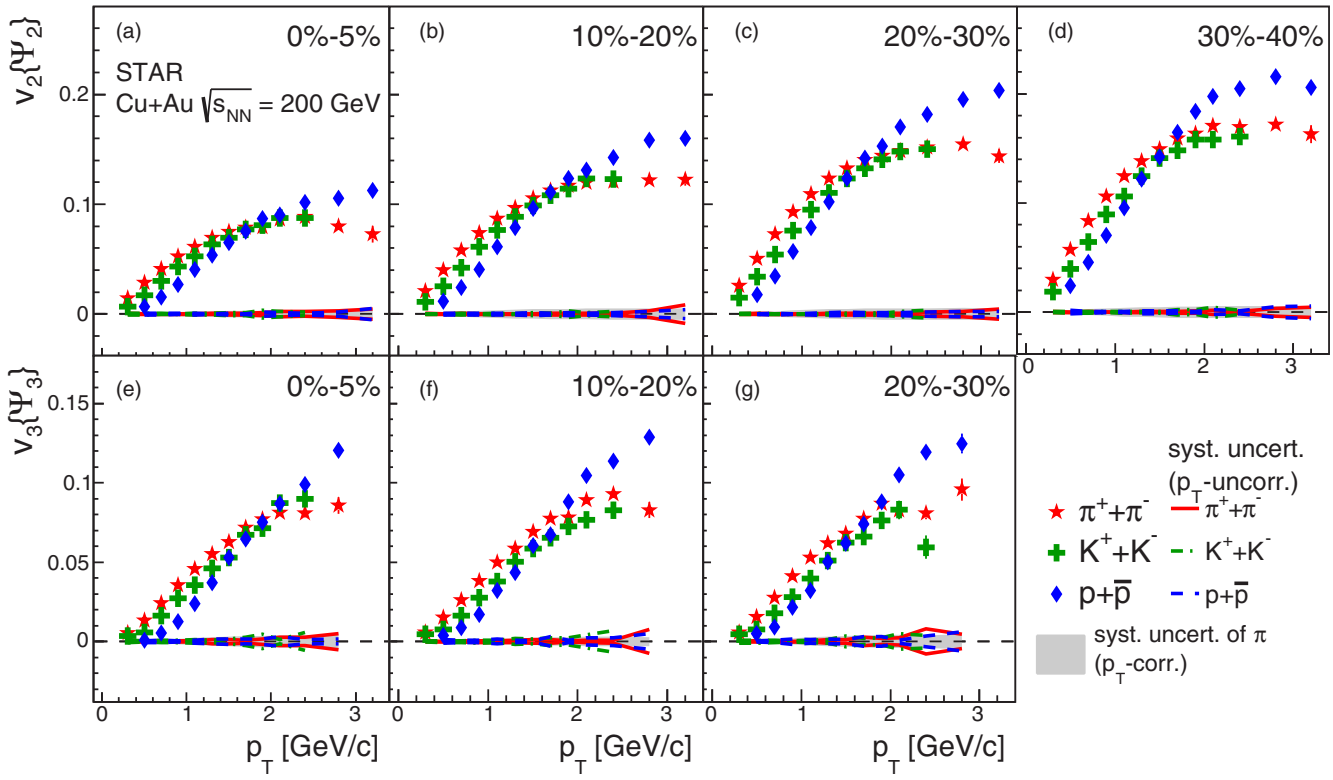

FIG. 17. The second and third harmonic flow coefficients of $\pi^+ + \pi^-$, $K^+ + K^-$, and $p + \bar{p}$ as a function of p_T for four centrality bins. Solid lines represent p_T-uncorrelated systematic uncertainties for each species. Shaded bands represent p_T-correlated systematic uncertainties for pions.

presents v_2 and v_3 of $\pi^+ + \pi^-$, $K^+ + K^-$, and $p + \bar{p}$ for different centralities. A particle mass dependence is clearly seen at low transverse momenta ($p_T < 1.6$ GeV/c) similar to that seen in v_1 in Fig. 10. In the p_T range $1.6 < p_T < 3.2$ GeV/c, the splitting between baryons and mesons is observed in v_2 and v_3. Results for a wide centrality bin (0–40%) are shown in Fig. 18, along with results for v_4 that show similar trends to v_2 and v_3.

The baryon-meson splitting in the flow coefficients was already observed in symmetric collisions and indicates the

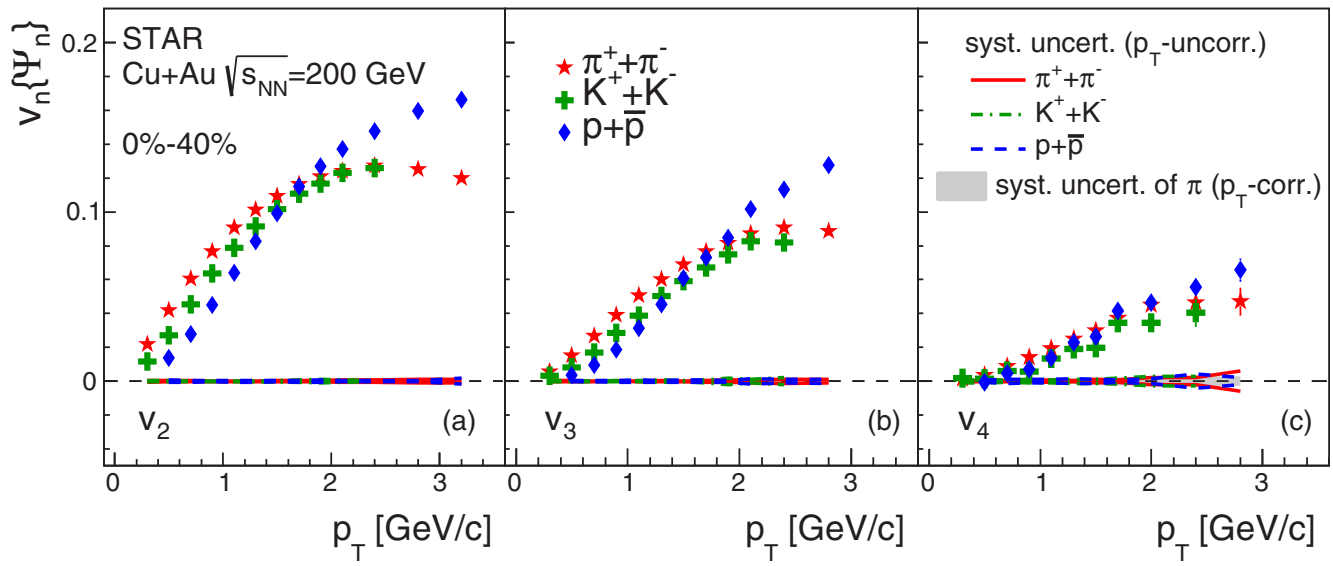

FIG. 18. Higher harmonic flow coefficients v_n of $\pi^+ + \pi^-$, $K^+ + K^-$, and $p + \bar{p}$ as a function of p_T in the 0–40% centrality bin. Solid lines represent p_T-uncorrelated systematic uncertainties for each species. Shaded bands represent p_T-correlated systematic uncertainties for pions.

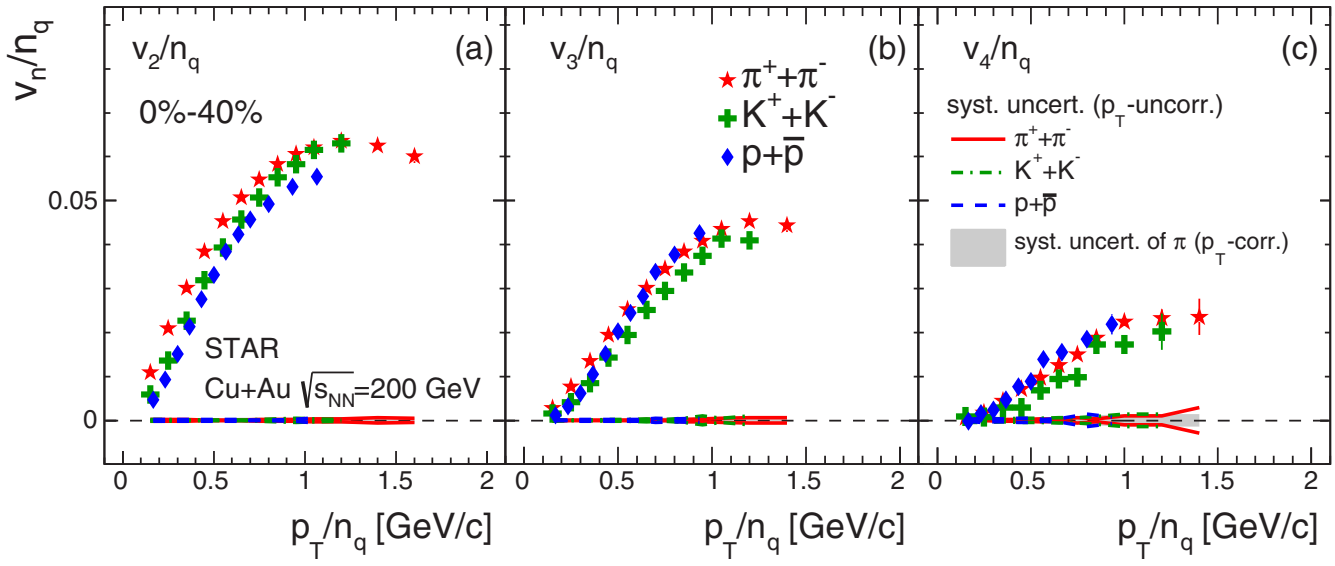

FIG. 19. NCQ scaling of v_2, v_3, and v_4 of $\pi^+ + \pi^-$, $K^+ + K^-$, and $p + \bar{p}$ as a function of p_T/n_q in the 0–40% centrality bin. Solid lines represent p_T-uncorrelated systematic uncertainties for each species. Shaded bands represent p_T-correlated systematic uncertainties for pions.

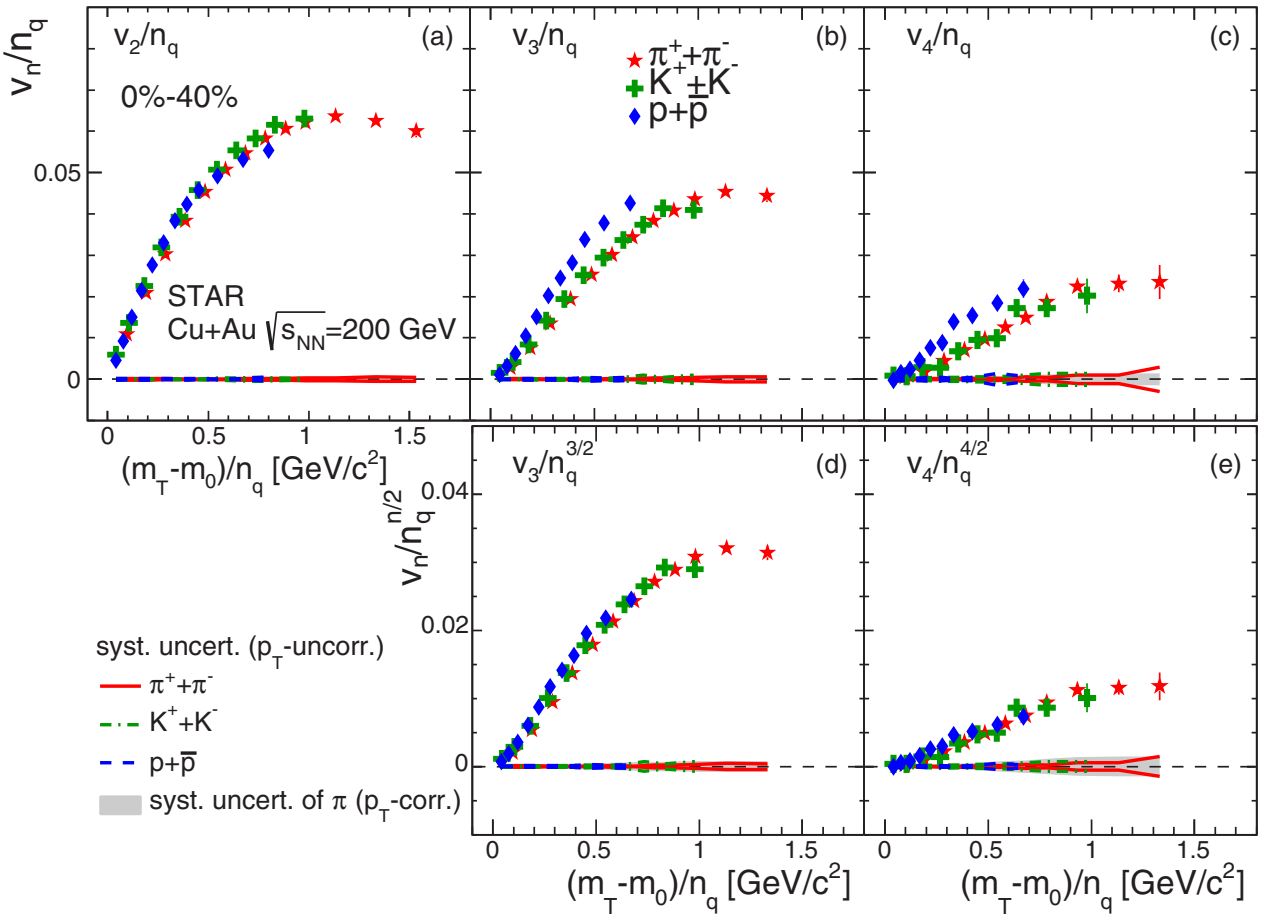

FIG. 20. NCQ scalings of v_2, v_3, and v_4 of $\pi^+ + \pi^-$, $K^+ + K^-$, and $p + \bar{p}$ as a function of $(m_T - m_0)/n_q$ in the 0–40% centrality bin. Solid lines represent p_T-uncorrelated systematic uncertainties for each species. Shaded bands represent p_T-correlated systematic uncertainties for pions.

collective flow at a partonic level, which can be tested by the number of constituent quark (NCQ) scaling. The idea of the NCQ scaling is based on the quark coalescence picture of hadron production in intermediate p_T [63,64]. In this process, hadrons at a given p_T are formed by n_q quarks with transverse momentum p_T/n_q, where $n_q = 2$ (3) for mesons (baryons). Figures 19(a)–19(c) show v_n/n_q for $\pi^+ + \pi^-$, $K^+ + K^-$, and $p + \bar{p}$ as a function of p_T/n_q. The scaled v_2, v_3, and v_4 as a function of p_T/n_q seem to follow a global trend for all particles species, although there are slight differences for each v_n. For example, the pion v_2 seems to deviate slightly from the other particles at low p_T region. This difference might be due to the effect of resonance decays or related to the nature of pions as Goldstone bosons [65,66]. Unlike the v_2, kaons seem to deviate from the other particles in v_3 and v_4.

An empirical NCQ scaling with the transverse kinetic energy, defined as $m_T - m_0$, is known to work well for v_2 [29,30]. m_T is defined as $m_T = \sqrt{p_T^2 + m_0^2}$ and m_0 denotes the particle mass. The idea of the NCQ scaling with the transverse kinetic energy comes from an attempt to account for the mass dependence of p_T shift during the system radial expansion. Figures 20(a)–20(c) show the NCQ scaling with the transverse kinetic energy for v_n in 0–40% centrality bin. The scaling works well for v_2 as reported in past studies for symmetric collisions [27,67], but it does not work for higher harmonics. A modified NCQ scaling for higher harmonics, $v_n/n_q^{n/2}$, was proposed in Ref. [68]. It works better for v_3 and v_4, as seen in Figs. 20(d) and 20(e), as it did in Au+Au collisions [31]. Hadronic rescattering might be responsible for the modified scaling, but the underlying physics is still under discussion [69,70].

VI. SUMMARY

We have presented results of azimuthal anisotropic flow measurements, from first-order up to fourth-order harmonics, for unidentified and identified charged particles in Cu+Au collisions at $\sqrt{s_{NN}} = 200$ GeV, as well as the directed flow of charged particles in Au+Au collisions at $\sqrt{s_{NN}} = 200$ GeV from the STAR experiment. In addition to directed flow, the average projection of the transverse momentum on the flow direction, $\langle p_x \rangle$, was measured in the both systems.

For inclusive charged particles, the directed flow v_1 was measured as functions of η and p_T over a wide centrality range. The slope of the conventional $v_1(\eta)$ in Cu+Au is found to be similar to that in Au+Au, but is shifted toward the forward rapidity (the Cu-going direction), while the $\langle p_x \rangle$ in Cu+Au has a slightly steeper slope and is shifted towards backward rapidity (the Au-going direction). The similar slopes of v_1 likely indicate a similar initial tilt of the created medium. Such a tilt seems to depend weakly on the system size but does depend on the collision energy. The slight difference in slope of $\langle p_x \rangle$ could be explained by the momentum balance of particles between the forward and backward rapidities and the asymmetry in multiplicity distribution over η in Cu+Au collisions. The shift of the intercept in $\langle p_x \rangle$ is close to the expectation based on the shift in the center-of-mass rapidity estimated by the number of participants in Au and Cu nuclei in a Monte Carlo Glauber model [Eq. (15)]. Comparing slopes of $v_1(\eta)$ with those of $\langle p_x \rangle$, we conclude that in midcentral collisions the relative contribution to conventional directed flow from the initial tilt is about 2/3 with the rest coming from rapidity dependence of the initial density asymmetry. The fluctuation component of v_1 in Au+Au agrees with that in Pb+Pb collisions at $\sqrt{s_{NN}} = 2.76$ TeV and shows a weak centrality dependence. This indicates that the initial dipolelike fluctuations do not depend on the system size, the system shape (overlap region of the nuclei), or the collisions energy.

The mean transverse momentum projected onto the spectator plane $\langle p_x \rangle$ shows charge dependence in Cu+Au collisions but not in Au+Au collisions, similarly as observed in charge-dependent directed flow reported in our previous publication [11]. The observed difference can be explained by the initial electric field due to the charge difference in Cu and Au spectator protons. The charge-dependent $v_1(p_T)$ was also measured for pions, kaons, and (anti)protons. The pion results are very similar to our previous results of inclusive charged particles. The charge difference of v_1 for kaons and protons is no larger than that of pions and consistent with zero within larger experimental uncertainties. These results may indicate that the number of charges, i.e., quarks and antiquarks, at the early time when the electric field is strong ($t < 0.1$ fm/c) is smaller than the number of charges in the final state.

Higher harmonic flow coefficients, v_2, v_3, and v_4, were also presented as functions of p_T in various centrality bins, showing a similar centrality dependence to those in Au+Au collisions. The v_2 in Cu+Au is smaller than that in Au+Au for the same number of participants because of different initial eccentricities. Meanwhile, v_3 scales with the number of participants between both systems, supporting the idea that v_3 originates from density fluctuations in the initial state. For $p_T < 2$ GeV/c, v_2 and v_3 were found to be reasonably well reproduced by the event-by-event viscous hydrodynamic model with the shear viscosity to entropy density $\eta/s = 0.08$–0.16 with the Glauber initial condition. The AMPT model calculations also qualitatively reproduced the data of v_2, v_3, and v_4.

For identified particles, a particle mass dependence was observed at low p_T for all flow coefficients (v_1-v_4), and a baryon-meson splitting was observed at intermediate p_T for v_2, v_3, and v_4, as expected from the collective behavior at the partonic level. The number of constituent quark scaling with p_T, originating in a naive quark coalescence model, works within ~10% for all v_n. The empirical number of constituent quark scaling with the kinetic energy works well for elliptic flow but not for higher harmonics, where the modified scaling works better. This is similar to what has been observed in Au+Au collisions. The exact reason for that is still unknown; our new data should help in future theoretical efforts in answering this question.

ACKNOWLEDGMENTS

We thank the RHIC Operations Group and RCF at BNL, the NERSC Center at LBNL, and the Open Science Grid consortium for providing resources and support. This work

was supported in part by the Office of Nuclear Physics within the US DOE Office of Science, the US National Science Foundation, the Ministry of Education and Science of the Russian Federation, National Natural Science Foundation of China, Chinese Academy of Science, the Ministry of Science and Technology of China and the Chinese Ministry of Education, the National Research Foundation of Korea, Czech Science Foundation and Ministry of Education, Youth and Sports of the Czech Republic, Department of Atomic Energy and Department of Science and Technology of the Government of India, the National Science Centre of Poland, the Ministry of Science, Education and Sports of the Republic of Croatia, RosAtom of Russia and German Bundesministerium fur Bildung, Wissenschaft, Forschung and Technologie (BMBF), and the Helmholtz Association.

APPENDIX: DIRECTED FLOW FROM A TILTED SOURCE

In this Appendix we derive the relation between the rapidity slopes of v_1 and $\langle p_x \rangle$ in the tilted source scenario. The approach used here is very similar to the one developed in Ref. [52]. Let us denote the invariant particle distribution as

$$\frac{d^3n}{d^2p_T dy} = J_0(p_T, y). \tag{A1}$$

A small "tilt" in xz plane by an angle γ leads to a change in the x component of the momentum $\Delta p_x = \gamma p_z = \gamma p_T / \tan(\theta) = \gamma p_T \sinh\eta$, where η is the pseudorapidity. Then the particle distribution in a tilted coordinate system would read

$$\begin{aligned} J &\approx J_0 + \frac{\partial J_0}{\partial p_T}\frac{\partial p_T}{\partial p_x}\Delta p_x \\ &= J_0\left(1 + \frac{\partial \ln J_0}{\partial p_T}\cos\phi\ p_T\ \gamma\ \sinh\eta\right). \end{aligned} \tag{A2}$$

From here one gets

$$v_1(p_T) = \frac{1}{2}\gamma\ p_T \sinh\eta \frac{\partial \ln J_0}{\partial p_T}. \tag{A3}$$

Heavier particle spectra usually have less steep dependence on p_T, which would lead to the mass dependence of $v_1(p_T)$—particles with large mass would have smaller v_1 at a given p_T. Integrating over p_T, and using p_T weight for $\langle p_x \rangle$ calculation leads to the following ratio of slopes:

$$\frac{\frac{1}{p_T}\frac{d\langle p_x\rangle}{d\eta}}{\frac{dv_1}{d\eta}} = \frac{1}{p_T}\frac{\left\langle p_T^2 \frac{\partial \ln J_o}{\partial p_T}\right\rangle}{\left\langle p_T \frac{\partial \ln J_o}{\partial p_T}\right\rangle}. \tag{A4}$$

For both the exponential form of $J_0(p_T)$ (approximately describing the spectra of light particles) and the Gaussian form (better suited for description of protons), this ratio equals 1.5.

[1] S. Singha, P. Shanmuganathan, and D. Keane, The first moment of azimuthal anisotropy in nuclear collisions from AGS to LHC energies, Adv. High Energy Phys. **2016**, 2836989 (2016).

[2] U. Heinz and R. Snellings, Collective flow and viscosity in relativistic heavy-ion collisions, Annu. Rev. Nucl. Part. Sci. **63**, 123 (2013).

[3] S. A. Voloshin, A. M. Poskanzer, and R. Snellings, Collective phenomena in non-central nuclear collisions, in *Relativistic Heavy Ion Physics*, Landolt-Börnstein - Group I Elementary Particles, Nuclei and Atoms Vol. 23, edited by R. Stock (Springer-Verlag, Berlin, Heidelberg, 2010).

[4] C. Gale, S. Jeon, B. Schenke, P. Tribedy, and R. Venugopalan, Event-By-Event Anisotropic Flow in Heavy-Ion Collisions from Combined Tang-Mills and Viscous Fluid Dynamics, Phys. Rev. Lett. **110**, 012302 (2013).

[5] A. Adare *et al.* (PHENIX Collaboration), Measurements of Higher Order Flow Harmonics in Au+Au Collisions at $\sqrt{s_{NN}} =$ 200 GeV, Phys. Rev. Lett. **107**, 252301 (2011).

[6] L. Adamczyk *et al.* (STAR Collaboration), Global Λ hyperon polarization in nuclear collisions, Nature (London) **548**, 62 (2017).

[7] D. E. Kharzeev, J. Liao, S. A. Voloshin, and G. Wang, Chiral magnetic and vortical effects in high-energy nuclear collisions–A status report, Prog. Part. Nucl. Phys. **88**, 1 (2016).

[8] Y. Hirono, M. Hongo, and T. Hirano, Estimation of the electric conductivity of the quark gluon plasma via asymmetric heavy-ion collisions, Phys. Rev. C **90**, 021903 (2014).

[9] V. Voronyuk, V. D. Toneev, S. A. Voloshin, and W. Cassing, Charge-dependent directed flow in asymmetric nuclear collisions, Phys. Rev. C **90**, 064903 (2014).

[10] S. A. Voloshin and T. Niida, Ultra-relativistic nuclear collisions: Direction of spectator flow, Phys. Rev. C **94**, 021901(R) (2016).

[11] L. Adamczyk *et al.* (STAR Collaboration), Charge-Dependent Directed Flow in Cu+Au Collisions at $\sqrt{s_{NN}} = 200$ GeV, Phys. Rev. Lett. **118**, 012301 (2017).

[12] L. P. Csernai and D. Röhrich, Third flow component as QGP signal, Phys. Lett. B **458**, 454 (1999).

[13] V. K. Magas, L. P. Csernai, and D. D. Strottman, Initial state of ultrarelativistic heavy ion collisions, Phys. Rev. C **64**, 014901 (2001).

[14] P. Bożek and I. Wyskiel, Directed flow in ultrarelativistic heavy-ion collisions, Phys. Rev. C **81**, 054902 (2010).

[15] F. Becattini, G. Inghirami, V. Rolando, A. Beraudo, L. Del Zanna, A. De Pace, M. Nardi, G. Pagliara, and V. Chandra, A study of vorticity formation in high energy nuclear collisions, Eur. Phys. J. C **75**, 406 (2015).

[16] R. J. M. Snellings, H. Sorge, S. A. Voloshin, F. Q. Wang, and N. Xu, Novel Rapidity Dependence of Directed Flow in High-Energy Heavy Ion Collisions, Phys. Rev. Lett. **84**, 2803 (2000).

[17] U. W. Heinz and P. F. Kolb, Rapidity dependent momentum anisotropy at RHIC, J. Phys. G **30**, S1229 (2004).

[18] D. Teaney and L. Yan, Triangularity and dipole asymmetry in relativistic heavy ion collisions, Phys. Rev. C **83**, 064904 (2011).

[19] L. P. Csernai, G. Eyyubova, and V. K. Magas, New method for measuring longitudinal fuctuations and directed flow in ultrarelativistic heavy ion reactions, Phys. Rev. C **86**, 024912 (2012); **88**, 019902(E) (2013).

[20] E. Retinskaya, M. Luzum, and J. Y. Ollitrault, Directed Flow at Midrapidity in $\sqrt{s_{NN}} = 2.76$ TeV Pb+Pb Collisions, Phys. Rev. Lett. **108**, 252302 (2012).

[21] J. Adams *et al.* (STAR Collaboration), Directed flow in Au+Au collisions at $\sqrt{s_{NN}} = 62.4$ GeV, Phys. Rev. C **73**, 034903 (2006).

[22] B. I. Abelev *et al.* (STAR Collaboration), System-Size Independence of Directed Flow Measured at the BNL Relativistic Heavy-Ion Collider, Phys. Rev. Lett. **101**, 252301 (2008).

[23] L. Adamczyk *et al.* (STAR Collaboration), Directed Flow of Identified Particles in Au+Au Collisions at $\sqrt{s_{NN}} = 200$ GeV at RHIC, Phys. Rev. Lett. **108**, 202301 (2012).

[24] B. Abelev *et al.* (ALICE Collaboration), Directed Flow of Charged Particles at Midrapidity Relative to the Spectator Plane in Pb+Pb Collisions at $\sqrt{s_{NN}} = 2.76$ TeV, Phys. Rev. Lett. **111**, 232302 (2013).

[25] G. Aad *et al.* (ATLAS Collaboration), Measurement of the azimuthal anisotropy for charged particle production in $\sqrt{s_{NN}} =$ 2.76 TeV lead-lead collisions with the ATLAS detector, Phys. Rev. C **86**, 014907 (2012).

[26] K. Aamodt *et al.* (ALICE Collaboration), Harmonic decomposition of two-particle angular correlations in Pb-Pb collisions at $\sqrt{s_{NN}} = 2.76$ TeV, Phys. Lett. B **708**, 249 (2012).

[27] J. Adams *et al.* (STAR Collaboration), Azimuthal anisotropy in Au+Au collisions at $\sqrt{s_{NN}} = 200$ GeV, Phys. Rev. C **72**, 014904 (2005).

[28] B. Alver and G. Roland, Collision geometry fluctuations and triangular flow in heavy-ion collisions, Phys. Rev. C **81**, 054905 (2010); **82**, 039903(E) (2010).

[29] B. I. Abelev *et al.* (STAR Collaboration), Mass, quark-number, and $\sqrt{s_{NN}}$ dependence of the second and fourth flow harmonics in ultrarelativistic nucleus-nucleus collisions, Phys. Rev. C **75**, 054906 (2007).

[30] A. Adare *et al.* (PHENIX Collaboration), Scaling Propertoes of of Azimuthal Anisotropy in Au+Au and Cu+Cu Collisions at $\sqrt{s_{NN}} = 200$ GeV, Phys. Rev. Lett. **98**, 162301 (2007).

[31] A. Adare *et al.* (PHENIX Collaboration), Measurement of the higher-order anisotropic flow coefficients for identified hadrons in Au+Au collisions at $\sqrt{s_{NN}} = 200$ GeV, Phys. Rev. C **93**, 051902(R) (2016).

[32] C. Adler *et al.*, The RHIC zero degree calorimeters, Nucl. Instrum. Methods Phys. Res., Sect. A **461**, 337 (2001).

[33] W. J. Llope *et al.*, The STAR vertex position detector, Nucl. Instrum. Methods Phys. Res., Sect. A **759**, 23 (2014).

[34] M. Anderson *et al.*, The star time projection chamber: A unique tool for studying high multiplicity events at RHIC, Nucl. Instrum. Methods Phys. Res., Sect. A **499**, 659 (2003).

[35] W. J. Llope (STAR Collaboration), Multigap RPCs in the STAR experiment at RHIC, Nucl. Instrum. Methods Phys. Res., Sect. A **661**, S110 (2012).

[36] L. Adamczyk *et al.* (STAR Collaboration), Inclusive charged hadorn elliptic flow in Au+Au collisions at $\sqrt{s_{NN}} = 7.7$–39 GeV, Phys. Rev. C **86**, 054908 (2012).

[37] L. Adamczyk *et al.* (STAR Collaboration), Centrality dependence of identified particle elliptic flow in relativistic heavy ion collisions at $\sqrt{s_{NN}} = 7.7$–62.4 GeV, Phys. Rev. C **93**, 014907 (2016).

[38] H. Bichsel, A method to improve tracking and particle identification in TPCs and silicon detectors, Nucl. Instrum. Methods Phys. Res., Sect. A **562**, 154 (2006).

[39] Y. Xu *et al.*, Improving the dE/dx calibration of the STAR TPC for the high-pT hadron identification, Nucl. Instrum. Methods Phys. Res., Sect. A **614**, 28 (2010).

[40] L. Adamczyk *et al.* (STAR Collaboration), Elliptic flow of identified hadrons in Au+Au collisions at $\sqrt{s_{NN}} = 7.7$–62.4 GeV, Phys. Rev. C **88**, 014902 (2013).

[41] J. Barrette *et al.* (E877 Collaboration), Proton and pion production relative to the reaction plane in Au+Au collisions at 11A GeV/c, Phys. Rev. C **56**, 3254 (1997).

[42] C. A. Whitten (STAR Collaboration), The beam-beam counter: A local polarimeter at STAR, in *Polarized Ion Sources, Targets and Polarimetry - PSTP2007: 12th International Workshop*, AIP Conf. Proc. No. 980, edited by A. Kponou, Y. Makdisi, and A. Zelenski (AIP, Melville, NY, 2008), p. 390.

[43] C. E. Allgower *et al.* (STAR Collaboration), The STAR endcap electromagnetic calorimeter, Nucl. Instrum. Methods Phys. Res., Sect. A **499**, 740 (2003).

[44] A. M. Poskanzer and S. A. Voloshin, Methods for analyzing anisotropic flow in relativistic nuclear collisions, Phys. Rev. C **58**, 1671 (1998).

[45] G. Wang (STAR Collaboration), Incident-energy and system-size dependence of directed flow, J. Phys. G **34**, S1093 (2007).

[46] J. Adam *et al.* (ALICE Collaboration), Higher harmonic flow coefficients of identified hadrons in Pb-Pb collisions at $\sqrt{s_{NN}} =$ 2.76 TeV, J. High Energy Phys. 09 (2016) 164.

[47] C. Adler *et al.* (STAR Collaboration), Elliptic flow from two- and four-particle correlations in Au+Au collisions at $\sqrt{s_{NN}} =$ 130 GeV, Phys. Rev. C **66**, 034904 (2002).

[48] M. Luzum and J. Y. Ollitrault, Eliminating experimental bias in anisotropic-flow measurements of high-energy nuclear collisions, Phys. Rev. C **87**, 044907 (2013).

[49] P. Bożek, Event-by-event viscous hydrodynamics for Cu-Au collisions at $\sqrt{s_{NN}} = 200$ GeV, Phys. Lett. B **717**, 287 (2012).

[50] L. Adamczyk *et al.* (STAR Collaboration), Beam-Energy Dependence of the Directed Flow of Protons, Antiprotons, and Pions in Au+Au Collisions, Phys. Rev. Lett. **112**, 162301 (2014).

[51] S. A. Voloshin (E877 Collaboration), Anisotropic flow of identified particles in Au+Au collisions at AGS energy, Nucl. Phys. A **638**, 455c (1998).

[52] S. A. Voloshin, Transverse radial expansion and directed flow, Phys. Rev. C **55**, R1630 (1997).

[53] A. Adare *et al.* (PHENIX Collaboration), Measurements of directed, elliptic, and triangular flow in Cu+Au collisions at $\sqrt{s_{NN}} = 200$ GeV, Phys. Rev. C **94**, 054910 (2016).

[54] S. Pratt, Viewing the chemical evolution of the quark-gluon plasma with charge balance functions, PoS (CPOD 2013), 023 (2013).

[55] L. Adamczyk *et al.* (STAR Collaboration), Third harmonic flow of charged particles in Au+Au collisions at $\sqrt{s_{NN}} = 200$ GeV, Phys. Rev. C **88**, 014904 (2013).

[56] K. Aamodt *et al.* (ALICE Collaboration), Higher Harmonic Anisotropic Flow Measurements of Charged Particles in Pb-Pb Collisions at $\sqrt{s_{NN}} = 2.76$ TeV, Phys. Rev. Lett. **107**, 032301 (2011).

[57] B. Schenke, P. Tribedy, and R. Venugopalan, Initial-state geometry and fluctuations in Au+Au, Cu+Au, U+U collisions at energies available at the BNL Relativistic Heavy Ion Collider, Phys. Rev. C **89**, 064908 (2014).

[58] G. Aad *et al.* (ATLAS Collaboration), Measurement of the correlation between flow harmonics of different order in lead-lead collisions at $\sqrt{s_{NN}} = 2.76$ TeV with the ATLAS detector, Phys. Rev. C **92**, 034903 (2015).

[59] Z.-W. Lin, C. M. Ko, B.-A. Li, B. Zhang, and S. Pal, Multiphase transport model for relativistic heavy ion collisions, Phys. Rev. C **72**, 064901 (2005).

[60] X.-N. Wang and M. Gyulassy, HIJING: A Monte Carlo model for multiple jet production in pp, pA and AA collisions, Phys. Rev. D **44**, 3501 (1991).

[61] J. Xu and C. M. Ko, Triangular flow in heavy ion collisions in a multiphase transport model, Phys. Rev. C **84**, 014903 (2011).

[62] X. Sun, J. Liu, A. Schmah, S. Shi, J. Zhang, L. Huo, and H. Jiang, Elliptic and triangular flow of identified particles from the AMPT model at RHIC energies, J. Phys. G **42**, 115101 (2015).

[63] S. A. Voloshin, Anisotropic flow, Nucl. Phys. A **715**, 379c (2003).

[64] D. Molnar and S. A. Voloshin, Elliptic Flow at Large Transverse Momenta from Quark Coalescence, Phys. Rev. Lett. **91**, 092301 (2003).

[65] X. Dong, S. Esumi, P. Sorensen, N. Xu, and Z. Xu, Resonance decay effects on anisotropy parameters, Phys. Lett. B **597**, 328 (2004).

[66] V. Greco and C. M. Ko, Effects of resonance decays on hadron elliptic flows, Phys. Rev. C **70**, 024901 (2004).

[67] A. Adare *et al.* (PHENIX Collaboration), Systematic study of azimuthal anisotropy in Cu+Cu and Au+Au collisions at $\sqrt{s_{NN}} = 62.4$ and 200 GeV, Phys. Rev. C **92**, 034913 (2015).

[68] L. X. Han, G. L. Ma, Y. G. Ma, X. Z. Cai, J. H. Chen, S. Zhang, and C. Zhong, Initial fluctuation effect on harmonic flows in high-energy heavy-ion collisions, Phys. Rev. C **84**, 064907 (2011).

[69] C.-J. Zhang and J. Xu, Investigating the scaling of higher-order flows in relativistic heavy-ion collisions, Phys. Rev. C **93**, 024906 (2016).

[70] R. A. Lacey, A. Taranenko, J. Jia, N. N. Ajitanand, and J. M. Alexander, Scaling of the higher-order flow harmonics: implications for initial-eccentricity models and the "viscous horizon", arXiv:1105.3782.